nature chemical biology

ARTICLES

https://doi.org/10.1038/s41589-021-00915-2

Check for updates

Characterization of a patient-derived variant of GPX4 for precision therapy

Hengrui Liu[1], Farhad Forouhar[2], Tobias Seibt[3], Russell Saneto[4,5], Kristen Wigby[6,7], Jennifer Friedman[6,7,8,9], Xin Xia[10], Mikhail S. Shchepinov[11], Sanath Kumar Ramesh[12], Marcus Conrad[13,14] and Brent R. Stockwell[1,2,10,15] ✉

Glutathione peroxidase 4 (GPX4), as the only enzyme in mammals capable of reducing esterified phospholipid hydroperoxides within a cellular context, protects cells from ferroptosis. We identified a homozygous point mutation in the *GPX4* gene, resulting in an R152H coding mutation, in three patients with Sedaghatian-type spondylometaphyseal dysplasia. Using structure-based analyses and cell models, including patient fibroblasts, of this variant, we found that the missense variant destabilized a critical loop, which disrupted the active site and caused a substantial loss of enzymatic function. We also found that the R152H variant of GPX4 is less susceptible to degradation, revealing the degradation mechanism of the GPX4 protein. Proof-of-concept therapeutic treatments, which overcome the impaired R152H GPX4 activity, including selenium supplementation, selective antioxidants and a deuterated polyunsaturated fatty acid were identified. In addition to revealing a general approach to investigating rare genetic diseases, we demonstrate the biochemical foundations of therapeutic strategies targeting GPX4.

Sedaghatian-type spondylometaphyseal dysplasia (SSMD), first described in 1980, was reported as a rare neonatal lethal disorder characterized by severe metaphyseal chondrodysplasia with limb shortening, cardiorespiratory defects and central nervous system abnormalities[1]. Most infants with SSMD succumb within days after birth owing to respiratory distress[2]. To date, four SSMD-related *GPX4* variants have been described: c.476+5G>A, c.477-8_477-4del, c.270C>A (p.Tyr127*) and c.153_160del[3,4]. Considering the severe impact of these biallelic frameshifting or truncating mutations on GPX4 function, the clinical phenotypes of SSMD patients are probably due to complete loss of GPX4 enzymatic function, although the exact pathophysiological mechanism is unknown.

GPX4 is a selenoprotein and a member of the glutathione peroxidase family of enzymes, which share an antioxidant function of reducing peroxides through use of the cosubstrate glutathione[5]. Despite structural and functional similarities, GPX4 is distinct from other GPX enzymes, being the only enzyme in mammals capable of reducing esterified phospholipid hydroperoxides and cholesterol hydroperoxides within the context of cell membranes[5]. Therefore, when GPX4 activity is compromised, accumulation of lipid peroxidation products can disrupt membrane architecture, resulting in cell death through ferroptosis, an iron-dependent form of nonapoptotic cell death[6]. Accordingly, an essential role for GPX4 during embryogenesis and early development has been suggested by the failure of GPX4 homozygous knockout mice to survive past early gestation[7,8].

Here, using whole-exome sequencing, we identified three individuals with mild SSMD features from two unrelated families who were found to harbor a recurrent homozygous point mutation in the *GPX4* gene, c.455G>A (p. R152H). We sought to investigate the impact of this patient-derived *GPX4* missense variant on the function of GPX4 protein, to guide SSMD patients towards treatments. Furthermore, structural examination of the variant suggested that K48 has an essential role in modulating GPX4 function, in addition to the previously reported catalytic triad (Sec46/Gln81/Trp136) and Asn137 (ref. [9]). We further found that the R152H variant alters the degradation of GPX4, revealing the degradation mechanism of GPX4 protein.

Results

R152H variant causes substantial loss of function. A recurrent homozygous R152H point mutation in the *GPX4* gene was identified in the whole-exome sequencing of three patients with SSMD features (Supplementary Table 1). To investigate the impact of the R152H variant on GPX4 structure and function, we began with computational modeling of the $GPX4^{R152H}$ protein structure. Substitution of Arg152 by His in the crystal structure of GPX4 was followed by global minimization of the structure in an implicit solvent to generate a $GPX4^{R152H}$ structural model.

Comparing $GPX4^{R152H}$ with $GPX4^{WT}$, we found that the R152H variant substantially altered the surface around residue 152, as evidenced by the loss of a hydrophobic pocket centered on Arg152 in the wild-type (WT) protein (Fig. 1a). The change in the surface features mainly derived from a conformational change in the loop between Pro124 and Ala133, with which the long side chains of Arg152 formed multiple hydrogen bonds in the WT protein to

[1]Department of Chemistry, Columbia University, New York, NY, USA. [2]Herbert Irving Comprehensive Cancer Center, Columbia University, New York, NY, USA. [3]Department of Nephrology and Institute of Metabolism and Cell Death, Medizinische Klinik und Poliklinik IV, Klinikum der Universität München, Munich, Germany. [4]Division of Pediatric Neurology, Department of Neurology, University of Washington, Seattle, WA, USA. [5]Center for Integrative Brain Research, Seattle Children's Hospital, Seattle, WA, USA. [6]Department of Pediatrics, University of California, San Diego, CA, USA. [7]Rady Children's Institute for Genomic Medicine, Rady Children's Hospital-San Diego, San Diego, CA, USA. [8]Department of Neurosciences, University of California San Diego, La Jolla, CA, USA. [9]Division of Child Neurology, Rady Children's Hospital, San Diego, CA, USA. [10]Department of Biological Sciences, Columbia University, New York, NY, USA. [11]Retrotope Inc., Los Altos, CA, USA. [12]CureGPX4.org, Seattle, WA, USA. [13]Helmholtz Zentrum München, Institute of Metabolism and Cell Death, Neuherberg, Germany. [14]Laboratory of Experimental Oncology, Pirogov Russian National Research Medical University, Moscow, Russia. [15]Irving Institute for Cancer Dynamics, Columbia University, New York, NY, USA. ✉e-mail: bstockwell@columbia.edu

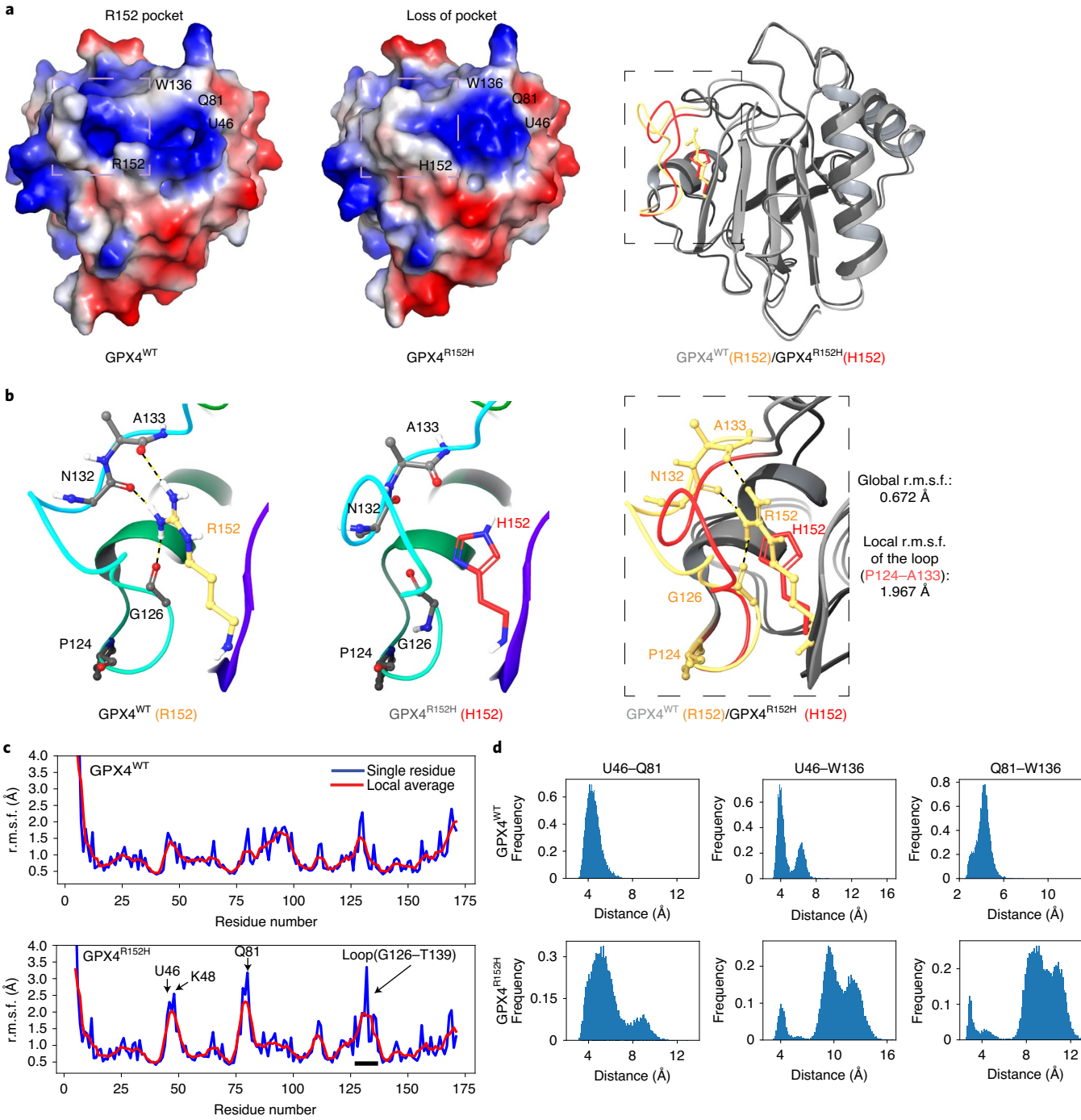

Fig. 1 | In silico analysis of the impact of R152H mutation on GPX4 structure (GPX4^{WT} PDB: 6HN3) predicted substantial conformational change and increased flexibility of the local loop and active site. a, The structure of GPX4^{R152H} was computationally modeled based on the crystal structure of GPX4^{WT} (PDB: 6HN3). Surface potential analysis of both the WT and R152H variant of GPX4 was conducted. Protein surfaces are colored as follows: hydrophobic (white), positive charge (red) and negative charge (blue). Overlap of the R152H variant backbone with WT is shown in the right-hand panel, where the major conformational change in the loop around His152 is shown (WT in yellow and R152H in red). **b**, Alteration of the surface mainly derived from an outstanding conformational change in the loop between Pro124 and Ala133, with which the side chains of Arg152 formed multiple hydrogen bonds in the WT, but not His152 in the mutant. **c**, Root mean squared fluctuation (r.m.s.f.) of each residue in MD simulations of GPX4^{R152H} and GPX4^{WT}. Representative data from three 100-ns trajectories were plotted. **d**, Distances between Sec46 and its catalytic partners Gln81/Trp136 were monitored in the MD simulation of GPX4^{R152H}, compared with GPX4^{WT}. Representative data from three 100-ns trajectories were plotted.

support the loop in an open conformation, but not in the His variant, which has a short side chain and fewer H-bond donors such that the loop collapsed (Fig. 1b).

Molecular dynamics (MD) simulations of GPX4^{R152H} and GPX4^{WT} predicted this loop to be exceptionally mobile in the context of the variant (Fig. 1c). GPX4^{R152H} also exhibits additional flex-

ibility in its active site (Supplementary Videos 1 and 2). Accordingly, the average distance between the active site catalytic residue Sec46 and its catalytic partners Gln81/Trp136 was substantially increased in GPX4^{R152H} and showed a considerably wide distribution over the timescale of the dynamics simulated, indicating a predicted weaker interaction among the catalytic triad (Fig. 1d).

As a control, GPX4^{R152R} was also generated by synonymous mutation of Arg152 to Arg using the same method. Substantial structural alterations caused by the R152H mutation were observed in a comparison of GPX4^{R152R} with GPX4^{R152H}, excluding artificial effects associated with the analysis (Extended Data Figs. 1 and 2a,b, and Supplementary Videos 3 and 4). In addition, the presence of water in the MD simulation box considerably increased the mobility of the G126–T139 loop in GPX4^{R152H} compared with water-free simulations, suggesting that water alone is not enough to restore hydrogen bonds to stabilize this loop (Supplementary Table 2 and Supplementary Videos 5 and 6).

To experimentally determine the impact of this variant in a human cell context, we established a cell model of the R152H mutation by stably overexpressing either green fluorescent protein (GFP)-tagged GPX4^{WT} or GFP-tagged GPX4^{R152H} in HT-1080 fibrosarcoma cells, in which GPX4 functions to protect cells from ferroptosis (Extended Data Fig. 3a). Using HT-1080 cells transfected with empty vector as a control, we measured the enzymatic activity of the transfected GFP–GPX4 protein via its ability to reduce a phospholipid hydroperoxide in an NADPH (reduced nicotinamide adenine dinucleotide phosphate)-coupled assay, as reported previously[10]. By normalizing enzyme activity to protein level, as measured by western blotting, we found that one unit of GPX4^{R152H} exhibited ~40% of the activity of GPX4^{WT} in this scenario (Fig. 2a and Extended Data Fig. 3b,c). To further confirm the variant-induced loss of activity in different genetic backgrounds and exclude interference from endogenous WT GPX4, using *Gpx4*-knockout HT-1080 human cells and Pfa1 murine cells, we overexpressed human or murine, WT or R152H exogenous GPX4 (refs. [7,11–13]). We found that *Gpx4*-knockout cells expressing GPX4^{R152H}, similar to Gpx4-knockout cells, require α-tocopherol for normal growth, as they started to exhibit lower viability on day 7 after removal of α-tocopherol from the cell culture media, which is not the case for cells expressing GPX4^{WT}; this suggests a profound impact of the R152H variant on GPX4 function (Fig. 2b). To characterize this effect further, we measured the GPX4 enzymatic activity of engineered *Gpx4*-knockout cells cultured in medium with or without α-tocopherol and found an increasing loss of activity over time for R152H GPX4 without α-tocopherol (Fig. 2c and Extended Data Fig. 3d). Because the observed gradual loss of activity specifically for R152H GPX4 is correlated with the cell death timeline and is in advance of the decrease in viability, it suggests that the accumulation of lipid peroxides caused by the less active R152H GPX4 will further deactivate R152H GPX4 and that incremental loss of activity eventually leads to compromised cell viability.

We therefore predicted that the characteristic reduction in enzyme activity in R152H GPX4 would result in impaired resistance to ferroptosis. Accordingly, we tested the ferroptosis sensitivity of HT-1080 cells overexpressing comparable levels of GFP–GPX4^{WT} or GFP–GPX4^{R152H} (Extended Data Fig. 4a). Although both cell lines were more resistant to ferroptosis induced by the GPX4 inhibitors RSL3 and ML162 and by the system x_c^- inhibitor imidazole ketone erastin (IKE), compared with a cell line transfected with empty vector, overexpression of GPX4^{R152H} was less protective against ferroptosis inducers than was GPX4^{WT}, consistent with the lower activity of this variant protein for reducing lipid hydroperoxides (Fig. 2d).

These data suggest that the partial loss of GPX4 phospholipid peroxidase activity caused by R152H alteration probably contributes to the overall pathological phenotype in SSMD patients harboring this variant. Additionally, because a relatively low level of cellular GPX4 activity provided by a small amount of WT GPX4 was reported to be sufficient for cell survival in some contexts, R152H-specific vulnerability to deactivation by accumulation of lipid peroxide indicates a sensitivity of R152H GPX4 to overoxidation and therefore differentiates the lower activity of R152H GPX4 from equivalent activity provided by the WT GPX4 (ref. [13]). Beyond the observed activity loss, considering the profound impact of R152H on GPX4, we suspect that R152H may also impact GPX4 function through additional mechanisms.

R152H causes substantial conformational change. To further understand why the alteration of a single amino acid residue distant from the active site caused a significant loss of enzymatic function in GPX4, we solved the X-ray crystal structure of GPX4^{U46C} and GPX4^{U46C_R152H} at 1.5 Å resolution (Extended Data Fig. 4b,c). The backbone of GPX4^{U46C_R152H} aligned well with GPX4^{U46C}, and the most outstanding change was in the loop between Pro124 and Ala133, which was intrinsically disordered in GPX4^{R152H}, as evidenced by the loss of electron density corresponding to these residues (Fig. 2e,f). As modeling has suggested, this change is probably due to the loss of multiple hydrogen bonds that Arg152 forms with the backbone carbonyls of Gly126, Asn132 and Ala133, such that the loop becomes exceptionally flexible when this arginine is not present. This change is consistent with our observation that GPX4^{U46C_R152H} exhibited a lower melting temperature than GPX4^{U46C} ($\Delta T_m = -4$ °C), which suggested R152H resulted in a conformational change in the GPX4 structure and substantially decreased the thermal stability of GPX4 protein (Fig. 2g).

Moreover, because active site residue Trp136 is in this disordered loop, we examined the active site and found distances between pairs of the catalytic residues were increased, as expected from modeling

Fig. 2 | R152H mutation resulted in a partial loss of function and structural change in GPX4. a, Using HT-1080 transfected with pBP empty vector as the control, the activity of WT or R152H GFP-tagged cytosolic GPX4 in HT-1080 cells was measured in an NADPH-coupled GPX4 activity assay and then normalized with the western blot intensity of GFP–GPX4. Data are plotted as means ± s.d. of six replicates. Ordinary one-way ANOVA followed by Tukey's multiple comparisons test was performed ($n = 6$, d.f. = 15). *P* values were plotted. **b**, Viabilities of *Gpx4*-knockout Pfa1 cells overexpressing exogenous human WT or R152H GPX4 (OE hGPX4), *Gpx4*-knockout Pfa1 cells overexpressing exogenous murine WT or R152H mScarlet-tagged GPX4, and *Gpx4*-knockout HT-1080 cells overexpressing exogenous murine WT or R152H mScarlet-tagged GPX4 (OE mGPX4) were measured on day 5 and day 7 after removal of α-tocopherol from cell media. **c**, Activity of GPX4 in Gpx4-knockout cells overexpressing exogenous WT or R152H GPX4 was measured on day 0 and day 5 after removal of α-tocopherol from cell media. Data are plotted as means ± s.d., $n = 5$ biologically independent samples for day 0 (left), and $n = 4$ biologically independent samples for day 5 (right). See 'Cell lines' section of Methods for discussion on effects of α-tocopherol. **d**, Viabilities of HT-1080 overexpressing exogenous WT or R152H GFP–GPX4 and a control line were measured after treatment with RSL3 (62.5 nM), ML162 (62.5 nM) and IKE (0.3 μM) for 48 h. Data are plotted as means ± s.d. ($n = 3$ biologically independent samples). Two-tailed *t*-tests were performed and *P* values plotted. **e**, The crystal structure of GPX4^{U46C_R152H}. Loss of electron density corresponding to the loop indicates a lack of fixed or ordered three-dimensional structure in this part of the protein. See Methods for rationale of using U46C GPX4. **f**, Overlap of GPX4^{U46C_R152H} with the GPX4^{U46C} also revealed a conformational change in Lys48, which is around the active site. The structure of GPX4^{U46C} that we solved is consistent with the previously reported structure (PDB: 2OBI). **g**, Melt temperatures of GPX4^{U46C_R152H} and GPX4^{U46C} were measured in the thermal shift assay with Sypro Orange as the reporter ($n = 12$ biologically independent samples).

(Extended Data Fig. 4d,e). Although this observation may partly explain the decrease in catalytic activity, we also noticed in the X-ray structure an outstanding shift of the side chain of Lys48 away from the active site (Extended Data Fig. 4f). The exceptional mobility of Lys48 was also predicted by modeling. Because the positively charged Lys48 features strong interactions with the active site selenium/sulfur anion in the structure of GPX4^{WT} and our MD simulation of GPX4^{U46C}, we reasoned that Lys48 might have an important role in the enzymatic function of GPX4, and its departure from the active site may impair enzymatic activity (Supplementary Video 7)[14].

Lys48 has an essential role in modulating GPX4 activity. To further investigate the role of Lys48 in the enzymatic function of GPX4, we generated HT-1080 cells stably overexpressing an alanine mutant of GPX4, GFP–GPX4^{K48A} or GFP–GPX4^{K48L}, in which the mutation removed the positively charged ε-amino group on the side chain. Strikingly, we found that GPX4^{K48A} had an almost complete loss of activity to reduce phospholipid hydroperoxides in this context, as its overexpression did not effectively increase overall GPX4 activity in HT-1080 cells, which is in contrast to the overexpression of WT GPX4 (Fig. 3a and Extended Data Fig. 5a). By contrast, we found

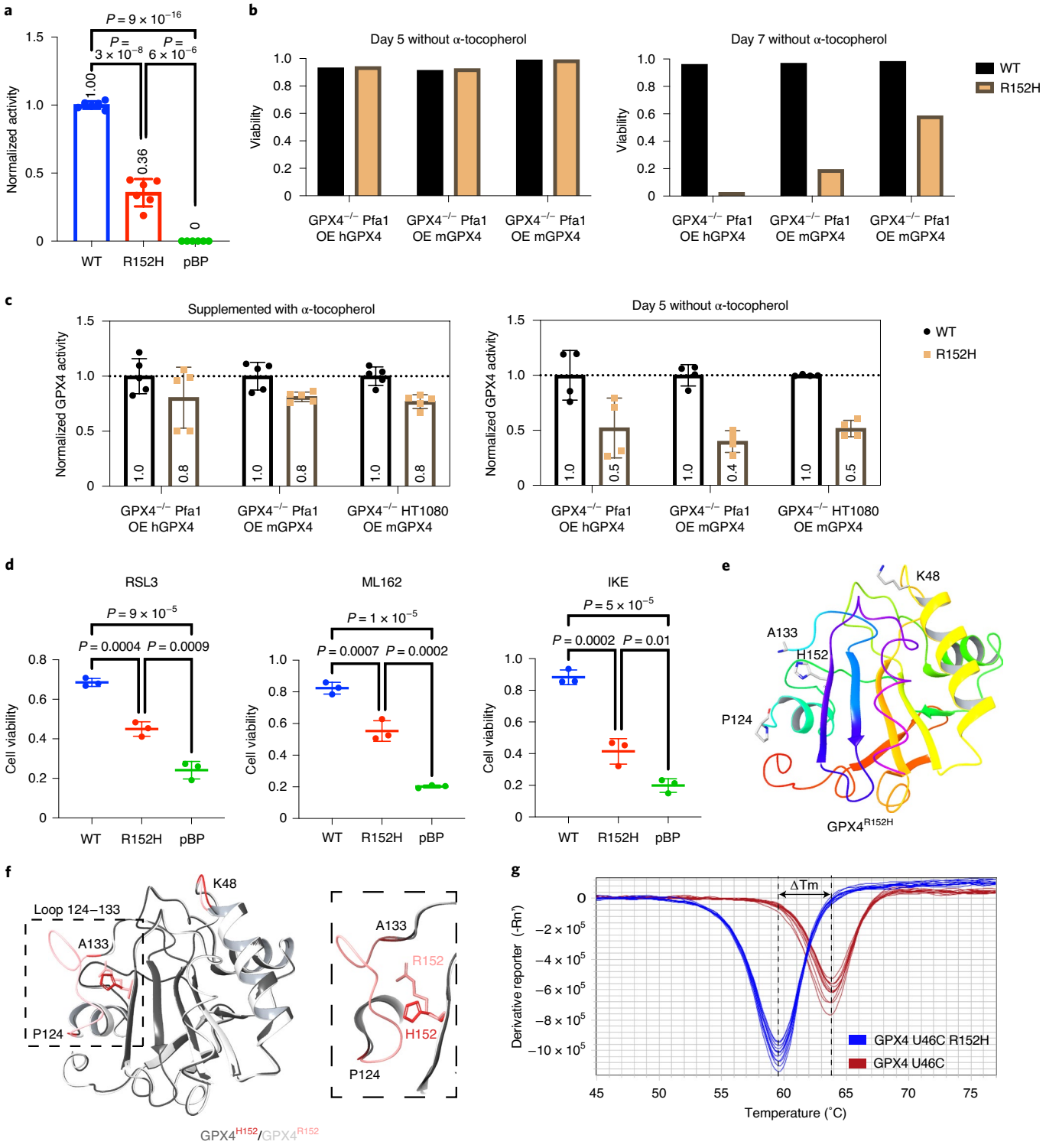

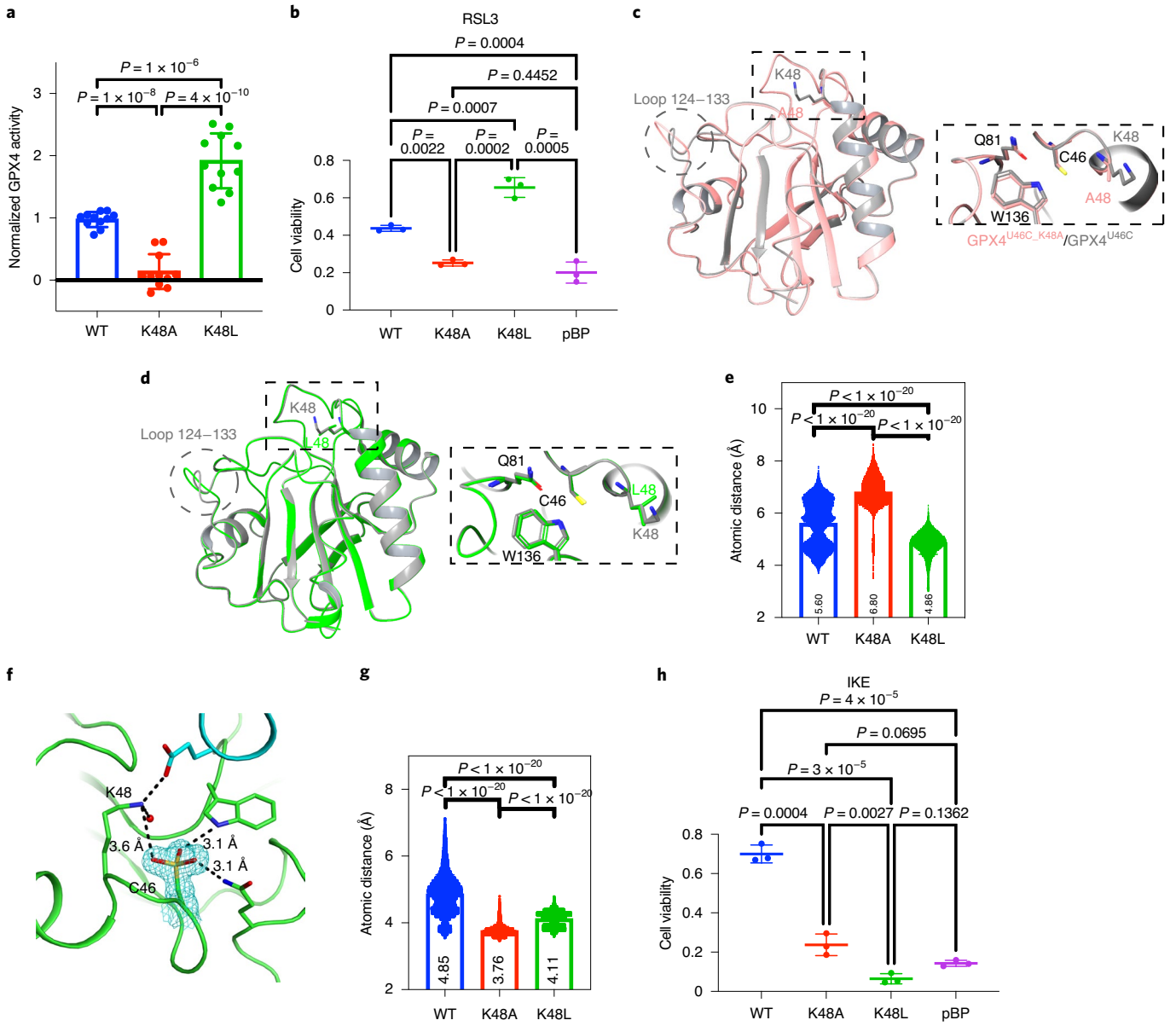

Fig. 3 | Lys48 modulates the enzymatic function of GPX4. a, Using HT-1080 transfected with pBP empty vector as a control, the activities of WT, K48A and K48L GFP-tagged cytosolic GPX4 were measured in an NADPH-coupled GPX4 activity assay. Data are plotted as means ± s.d. of 11 replicate experiments. Ordinary one-way ANOVA followed by Tukey's multiple comparisons test was performed ($n = 11$, d.f. = 30). *P* values were plotted. **b**, Viabilities of HT1080 overexpressing exogenous WT, K48A or K48L GFP–GPX4 and a control line were measured after treatment with RSL3 (62.5 nM) for 48 h. Data are plotted as means ± s.d. ($n = 3$ biologically independent samples). Two-tailed *t*-tests were performed and *P* values plotted. **c**, The crystal structure of $GPX4^{U46C\_K48A}$ aligned with that of $GPX4^{U46C}$. **d**, The crystal structure of $GPX4^{U46C\_K48L}$ aligned with that of $GPX4^{U46C}$. **e**, The distances between catalytic residues Cys46 and Trp136 were recorded every 4.8 ps for ten independent 100-ns MD simulations of $GPX4^{U46C}$, $GPX4^{U46C\_K48A}$ and $GPX4^{U46C\_K48L}$. All $n = 208{,}350$ independent measurements of distances throughout the ten independent simulations were plotted, with means ± s.d. An unpaired two-tailed *t*-test was then performed and *P* values plotted. **f**, In the crystal structure of oxidized $GPX4^{U46C}$ (Cys46-SO_3H), Lys48 is in close proximity to the oxidized Cys46. The F_o–F_c omit map (cyan mesh) contoured at 3σ. The side chain of E65 (cyan) belongs to protomer B. The solid red sphere represents a water molecule in the active site. **g**, The distances between catalytic residues Cys46 and Trp136 were recorded every 4.8 ps for five 100-ns MD simulations of oxidized $GPX4^{U46C}$, $GPX4^{U46C\_K48A}$ and $GPX4^{U46C\_K48L}$ (Cys46-SO_3H). All $n = 20{,}835$ independent measurements of distances over the simulation time were plotted, with means ± s.d. An unpaired two-tailed *t*-test was performed and *P* values plotted. **h**, Viabilities of HT1080 overexpressing exogenous WT, K48A or K48L GFP–GPX4 and a control line were measured after treatment with IKE (0.6 μM) for 48 h. Data are plotted as means ± s.d. ($n = 3$ biologically independent samples). Two-tailed *t*-tests were performed and *P* values plotted.

that $GPX4^{K48L}$ featured enhanced enzymatic activity, in line with a previous observation that the recombinant K48L mutant of GPX4 had higher catalytic activity than WT[14].

Correspondingly, although overexpression of GFP–$GPX4^{K48A}$ in HT-1080 cells did not show further protective effects in addition to endogenous GPX4 against ferroptosis induced by RSL3, overexpression of GFP–$GPX4^{K48L}$ was more protective than WT GPX4 against RSL3 (Fig. 3b and Extended Data Fig. 5b). These results suggested a profound and intriguing modulatory role of Lys48 on GPX4 activity.

To shed light on the mechanism for this essential modulation, we solved the crystal structures of $GPX4^{U46C\_K48A}$ and $GPX4^{U46C\_K48L}$ protein (Extended Data Fig. 5c,d). Although the $GPX4^{U46C\_K48A}$ and $GPX4^{U46C\_K48L}$ proteins are stable and superimpose well upon the structure of $GPX4^{U46C}$ (Fig. 3c,d), MD simulations of these three structures revealed additional flexibility in the active site of $GPX4^{U46C\_K48A}$, whereas enhanced stability was observed in the active site of $GPX4^{U46C\_K48L}$ (Supplementary Videos 7–9). Accordingly, the average distance between the active site catalytic residue Cys46 and its catalytic partner Trp136 was significantly increased in $GPX4^{U46C\_K48A}$, which indicated a weaker interaction, whereas the average distance in $GPX4^{U46C\_K48L}$ was even lower than in $GPX4^{U46C}$, which indicated a stronger interaction (Fig. 3e). Consistent results were also observed in MD simulations of computationally modeled Lys48 variants of WT selenocysteine-containing GPX4 (Extended Data Fig. 5e and Supplementary Videos 10–12). This suggests that the interaction between Lys48 and (seleno-)Cys46 modulates the conformation of the GPX4 active site and normally stabilizes the active site in a more compact and functional state, and that this feature is impaired when Lys48 is mutated to Ala.

To further study the role of Lys48 within the context of the canonical catalytic cycle of the GPX4 enzymatic reaction, in which the first step is oxidation of GPX4 by its hydroperoxides substrates, we solved the crystal structure of fully oxidized $GPX4^{U46C}$, where the sulfur of Cys46 was oxidized to sulfonic acid (SO_3H, Extended Data Fig. 5f). We found that Lys48 is positioned in close proximity (3.6 Å) to oxidized Cys46, even closer than to reduced Cys46 (5.2 Å) in the crystal structure of reduced $GPX4^{U46C}$ (Fig. 3f). This close proximity was also previously observed in the structure of oxidized selenocysteine-containing GPX4[14]. This suggests a role for Lys48 in modulation of the active site in the oxidized state of GPX4. To further investigate this interaction, we performed MD simulations for fully oxidized $GPX4^{U46C}$, $GPX4^{U46C\_K48A}$ and $GPX4^{U46C\_K48L}$, and found that oxidized $GPX4^{U46C}$ exhibited additional flexibility in the active site, which suggests that the oxidized active site is in an open state. However, oxidized $GPX4^{U46C\_K48A}$ and $GPX4^{U46C\_K48L}$ featured extreme stability (Fig. 3g and Supplementary Videos 13–15). Because the SeO_3^-/SO_3^- state of GPX4 is inactive and irreversibly overoxidized, especially for the sulfur variant[11], the stability of the K48A mutant in this state might contribute to its loss of activity.

The second step in the catalytic cycle of GPX4 is the incorporation of its cofactor reduced glutathione (GSH) via formation of an Se–S bond, which prepares oxidized GPX4 for regeneration to the reduced form. Therefore, we covalently docked GSH into the crystal structures of $GPX4^{U46C}$, $GPX4^{U46C\_K48A}$, $GPX4^{U46C\_K48L}$ and the computationally modeled structures for Lys48 variants of WT GPX4. The highest covalent-docking affinities were obtained with $GPX4^{U46C}$ or $GPX4^{WT}$, both of which featured Lys48 (Extended Data Fig. 6a and Supplementary Table 3)[15]. This is in line with a previous study that proposed a role for Lys48 in interacting with GSH[16]. In addition, the flexible and open active site of oxidized $GPX4^{U46C}$, as found during its MD simulation, might also be more accessible for GSH to incorporate and reduce oxidized GPX4.

The above analysis suggested an elevated susceptibility of K48L to overoxidation, in spite of its higher initial activity, because loss of the positively charged ε-amino group in the K48L mutant might have an impact on its interaction with the negatively charged oxidized active site or the GSH cofactor. To validate our analysis, we tested the sensitivity of HT1080 cells overexpressing comparable levels of GFP–$GPX4^{WT}$ or GFP–$GPX4^{K48L}$ with ferroptosis induced by system x_c^- inhibitor IKE, which depleted cellular GSH and may therefore cause overoxidation of GPX4. We found that overexpression of GFP–$GPX4^{K48L}$ in HT1080 cells did not show further protective effects in addition to the endogenous GPX4 against IKE (Fig. 3h and Extended Data Fig. 6b).

In addition to K48A and K48L, we computationally modeled additional Lys48 variants of WT GPX4 and performed the above analysis on K48E (negative charge), K48Q (hydrogen bond) and K48R (positive charge and hydrogen bond). The broad performance spectrum observed with these Lys48 variants further supported the profound modulatory role of Lys48 in GPX4 activity (Extended Data Fig. 5e, Supplementary Table 3 and Supplementary Videos 16–18).

In summary, these data reveal a multipronged mechanism for the modulation of GPX4 enzymatic activity by Lys48: to stabilize the active site in a more compact and functional state, to modulate the oxidized active site for cycling and to facilitate incorporation of the cofactor GSH. Therefore, the shift in Lys48 away from the active site in $GPX4^{R152H}$ may contribute to the partial loss of function and specific sensitivity to overoxidation observed with $GPX4^{R152H}$.

R152H variant is resistant to degradation. When we tested the ferroptosis sensitivities of HT1080 cells overexpressing GFP–$GPX4^{R152H}$ or GFP–$GPX4^{WT}$, we were surprised to find that $GPX4^{R152H}$ provided protection comparable with $GPX4^{WT}$ to the ferroptosis inducer FIN56, despite insufficient protection against RSL3, ML162 and IKE (Fig. 4a and Extended Data Fig. 7a). Because FIN56 was reported to induce ferroptosis by promoting degradation of GPX4, as well as depleting coenzyme Q10 (CoQ_{10}) we speculated that R152H may change the susceptibility of GPX4 to degradation[17]. Therefore, we treated HT-1080 cells overexpressing GFP–$GPX4^{R152H}$ or GFP–$GPX4^{WT}$ with various ferroptosis inducers and measured the residual GPX4 protein after treatment by western blotting, using methods reported previously (Extended Data Fig. 7b)[18]. The endogenous GPX4 protein served as internal control and confirmed that RSL3, ML162 and FIN56 substantially promoted degradation of GPX4 under these treatment conditions (Fig. 4b and Extended Data Fig. 7c,d). Meanwhile, substantial degradation of transfected GFP–$GPX4^{WT}$ was induced by RSL3, ML162 and FIN56, as expected, which excluded interference of the GFP tag on the degradation (Fig. 4c and Extended Data Fig. 7e). We observed that GFP–$GPX4^{R152H}$ was more resistant than GFP–$GPX4^{WT}$ to degradation induced by RSL3, ML162 and FIN56 (Fig. 4d and Extended Data Fig. 7f). We further conducted cycloheximide-chase analyses of WT and R152H GFP–GPX4 under RSL3 treatment, which verified the increased half-life of R152H GPX4 under this condition (Fig. 4e and Extended Data Fig. 8a).

The mechanism of GPX4 degradation induced by RSL3 and FIN56 is not clear, despite efforts to understand this phenomenon[17,19]. Based on our finding that the loop between Pro124 and Ala133, which contains Lys125 and Lys127, exhibits extra flexibility in the context of $GPX4^{R152H}$, we developed a hypothesis that RSL3- or FIN56-induced GPX4 degradation involves a proteasome-dependent mechanism, with Lys125 and Lys127 as potential ubiquitination sites on GPX4; in this model, these highly mobile lysine residues in R152H hinder ubiquitination and prevent degradation. We tested this hypothesis by examining GPX4 degradation in HT1080 cells stably overexpressing GFP–$GPX4^{K125R\_K127R}$, in which the proposed sites of ubiquitin ligation were removed by point mutations. Whereas endogenous GPX4 was degraded upon treatment with RSL3, ML162 or FIN56, we found that GFP–$GPX4^{K125R\_K127R}$ was resistant to degradation, even more so than the R152H mutant (Fig. 4f and Extended Data Fig. 8b,c). Together, these data suggest that degradation of GPX4 induced by RSL3 and FIN56 involves a proteasome-dependent mechanism, and that Lys125 and Lys127 of GPX4 are key sites of ubiquitination. An alternative approach to modulate GPX4 for clinical applications was thus revealed.

Impact of R152H variant is similar in patient fibroblasts. To validate our observations regarding the R152H variant, fibroblasts developed from a patient with homozygous R152H variants

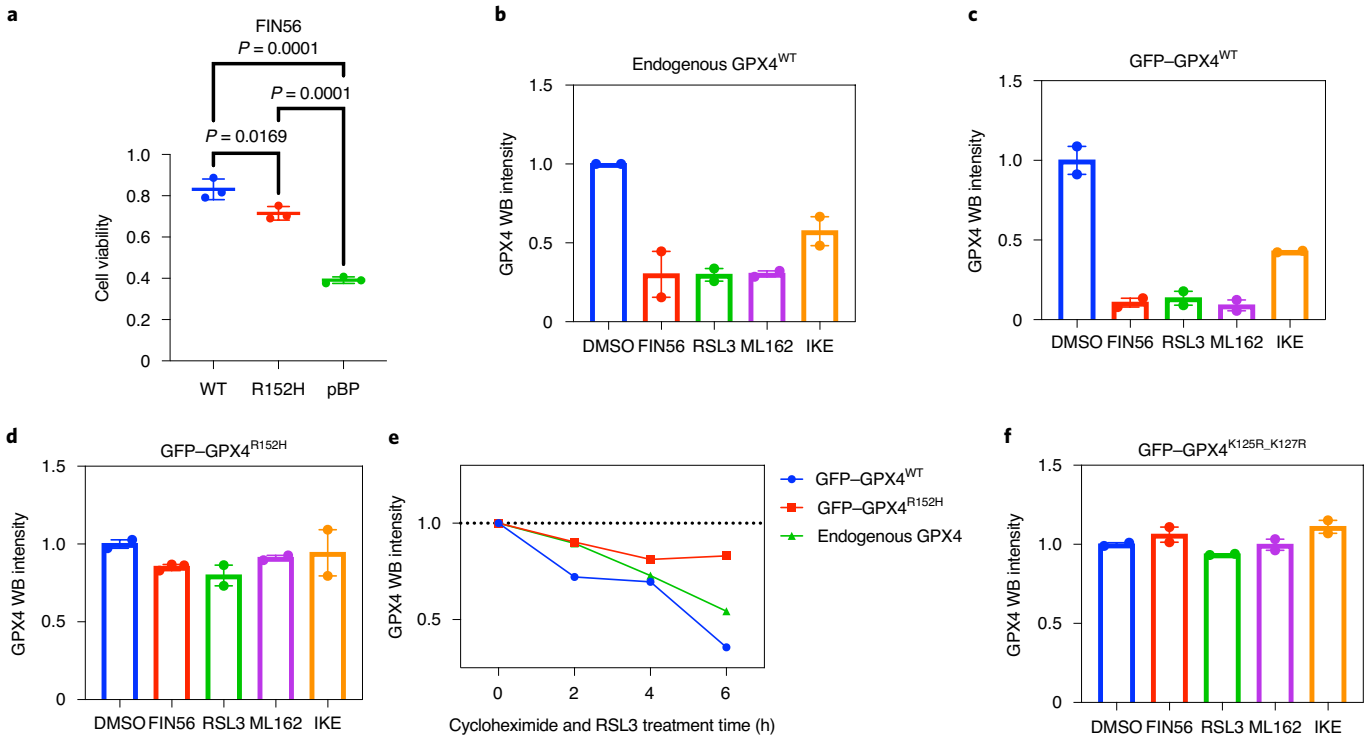

Fig. 4 | Resistance of GPX4^{R152H} to degradation induced by GPX4 inhibitor revealed the ubiquitin/proteosome-dependent mechanism of the GPX4 degradation induced by FIN56/RSL3. a, Viabilities of HT-1080 cells overexpressing exogenous WT or R152H GFP-GPX4 and a control line were measured after treatment with FIN56 (0.6 μM) for 48 h. Data are plotted as means ± s.d. ($n = 3$ biologically independent samples). Two-tailed *t*-tests were then performed for comparison and *P* values plotted. **b**, Endogenous GPX4 in HT1080 cells overexpressing GFP-GPX4^{WT} were tested for vulnerability to degradation induced by RSL3, ML162, FIN56 and IKE. Data are plotted as means with range of two biologically independent experiments. The corresponding blots are shown in Extended Data Fig. 4b,c. **c**, GFP-GPX4^{WT} in HT1080 cells overexpressing GFP-GPX4^{WT} was tested for vulnerability to degradation induced by RSL3, ML162, FIN56 and IKE. Data are plotted as means with range of two biologically independent experiments. The corresponding blots are shown in Extended Data Fig. 4e. **d**, GFP-GPX4^{R152H} in HT1080 cells overexpressing GFP-GPX4^{R152H} was tested for vulnerability to degradation induced by RSL3, ML162, FIN56 and IKE. Data are plotted as means with range of two biologically independent experiments. The corresponding blots are shown in Extended Data Fig. 4f. **e**, Cycloheximide-chase analysis of GFP-GPX4^{WT}, GFP-GPX4^{R152H} and endogenous WT GPX4. Means of two biologically independent experiments were plotted. The corresponding blots are shown in Extended Data Fig. 4g. **f**, GFP-GPX4^{K125R_K127R} in HT1080 cells overexpressing GFP-GPX4^{K125R_K127R} was tested for vulnerability to degradation induced by RSL3, ML162, FIN56 and IKE. Data are plotted as means with range of two biologically independent experiments. The corresponding blots are shown in Extended Data Fig. 4h. DMSO, dimethylsulfoxide; WB, western blotting.

(RAG01, GPX4$^{R152H/R152H}$) and the patient's parent as an unaffected control with heterozygous genotype (RAG02, GPX4$^{R152H/WT}$) were tested. Although the two human fibroblast cell lines expressed an equivalent level of GPX4 protein based on western blot analysis, RAG01 cells exhibited significantly less GPX4 enzymatic activity than RAG02, confirming that R152H variant in GPX4 caused partial loss of enzymatic function (Fig. 5a,b). As expected, RAG01 with a partial loss of GPX4 activity was found to be more sensitive than RAG02 to lipid peroxidation and to ferroptosis induced by RSL3, ML162, IKE and FIN56 (Fig. 5c).

We then tested the degradation vulnerability of GPX4 protein in both fibroblast cell lines, and found that the R152H variant altered the degradation of GPX4, such that GPX4^{R152H} in RAG01 was more resistant than the combination of GPX4^{WT} and GPX4^{R152H} in RAG02 to degradation induced by RSL3 and ML162, further suggesting the involvement of a ubiquitin–proteasome system in GPX4 degradation (Fig. 5d). Moreover, imaging of fibroblast cells with GPX4 immunofluorescence and 4,6-diamidino-2-phenylindole (DAPI) staining under confocal microscopy showed an indistinguishable level of cellular GPX4 intensity in RAG01 and RAG02 (Fig. 5e). In addition, the ratio of cytoplasmic GPX4 to nuclear GPX4 was comparable in RAG01 and RAG02, indicating that alteration of the GPX4 subcellular localization was not observed for this patient-derived variant (Fig. 5f,g). However, we found that cells undergoing mitosis exhibited a much higher fluorescence intensity for GPX4 than nonmitotic cells. This indicated that, during proliferation, fibroblast cells express a high level of GPX4 protein to protect themselves against lipid peroxidation. The loss-of-activity variant in GPX4 might therefore partially suppress mitosis or cause cell death during mitosis, as evidenced by the lower number of RAG01 cells than RAG02 cells when seeded equivalently.

Identification of proof-of-concept treatment. The above results demonstrated that the patient-derived R152H variant of GPX4 caused a partial loss of function in phospholipid peroxidase activity and therefore is pathological. However, the data also suggested that overexpression of the partially active but degradation-resistant GPX4^{R152H} in HT-1080 cells did increase the resistance of cells to ferroptosis induced by lipid peroxidation, although less effectively than WT GPX4 (Fig. 2d). Therefore, we developed a hypothesis that boosting expression of the R152H variant of the selenoprotein GPX4 via selenium supplementation might compensate for the partial loss of enzymatic function. This is based on the observation that selenium supplementation can effectively increase expression of the selenoprotein GPX4, up to 48-fold, as well as expression of another antioxidant selenoprotein, GPX1, up to 40-fold, in human cells[20]. In

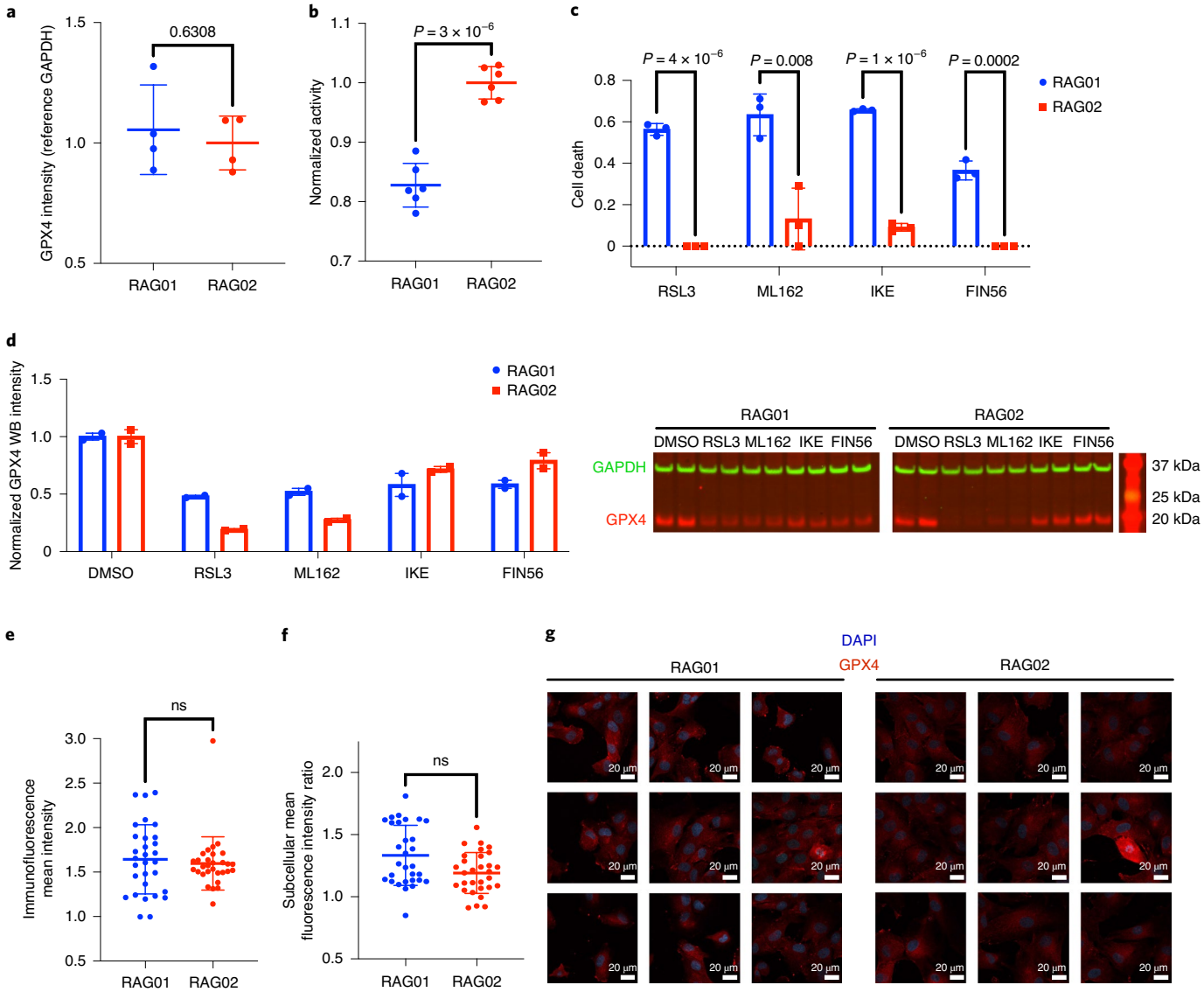

Fig. 5 | Pathology analysis was validated in the patient fibroblasts. a, RAG01 (patient, with homozygous R152H mutation in GPX4) and RAG02 (parent of patient, with heterozygous R152H mutation in GPX4) were tested for GPX4 protein expression level by western blotting. Data are plotted as means ± s.d. ($n = 4$ biologically independent samples). An unpaired two-tailed t-test was then performed ($t = 0.5061$, d.f. = 6) and the P value was plotted. **b**, Activity of GPX4 in RAG01 and RAG02 was measured in an NADPH-coupled GPX4 activity assay. Data are plotted as means ± s.d. ($n = 6$ biologically independent samples). An unpaired two-tailed t-test was then performed ($t = 9.212$, d.f. = 10) and the P value was plotted. See 'Cell lines' section of Methods for a discussion on the effects of α-tocopherol. **c**, Viabilities of RAG01 and RAG02 were measured after treatment with RSL3 (4 μM), ML162 (4 μM), IKE (30 μM) and FIN56 (500 μM) for 24 h. Data were plotted as means ± s.d. ($n = 3$ biologically independent samples). An ordinary two-way ANOVA followed by Sidak's multiple comparisons test was performed and P values were plotted ($n = 3$, d.f. = 16). **d**, RAG01 and RAG02 were tested for vulnerability to GPX4 degradation induced by 10 μM RSL3, ML162, FIN56 and IKE. Data are plotted as means with range in the left-hand panel ($n = 2$ biologically independent samples). Western blots are shown in the right-hand panel. The full scan image is shown in the Supplementary Information. **e**, Mean cellular immunofluorescence of GPX4 observed in RAG01 and RAG02. Data are plotted as means ± s.d. ($n = 30$ biologically independent samples). An unpaired two-tailed t-test was performed and plotted ($t = 0.5155$, d.f. = 58, $P = 0.6081$). **f**, Ratio of mean cytoplasm immunofluorescence of GPX4 to mean nuclear immunofluorescence of GPX4 observed in RAG01 and RAG02. Data are plotted as means ± s.d. ($n = 30$ biologically independent samples). An unpaired two-tailed t-test was performed and plotted ($t = 1.846$, d.f. = 58, $P = 0.0713$). **g**, Nine representative immunofluorescence images for RAG01 and RAG02 showing DAPI (blue) and GPX4 fluorescence (red). Scale bar, 20 μm. DMSO, dimethylsulfoxide.

addition, selenium is readily available from dietary source such as Brazil nuts and as an over-the-counter supplement[21].

We first tested this selenium treatment hypothesis on fibroblasts derived from the patient. We found that sodium selenite, selenomethione and methylselenocysteine could boost the viability of patient fibroblast RAG01 slightly to 138%, 138% and 137%, with an EC_{50} (half maximal effective concentration) value of 0.8, 0.4 and 0.9 nM, respectively (Fig. 6a,b and Extended Data Fig. 9a). The similarity in the increased viability for these three seleno compound treatments suggested a consistency of selenium supplementation, and their shared low EC_{50} values indicated their high potencies as treatments. Because the CC_{50} (50% cytotoxic concentration) of sodium selenite toxicity (12 μM) was 15,000-fold higher than the its EC_{50}, toxicity avoidance should be manageable in patients, although

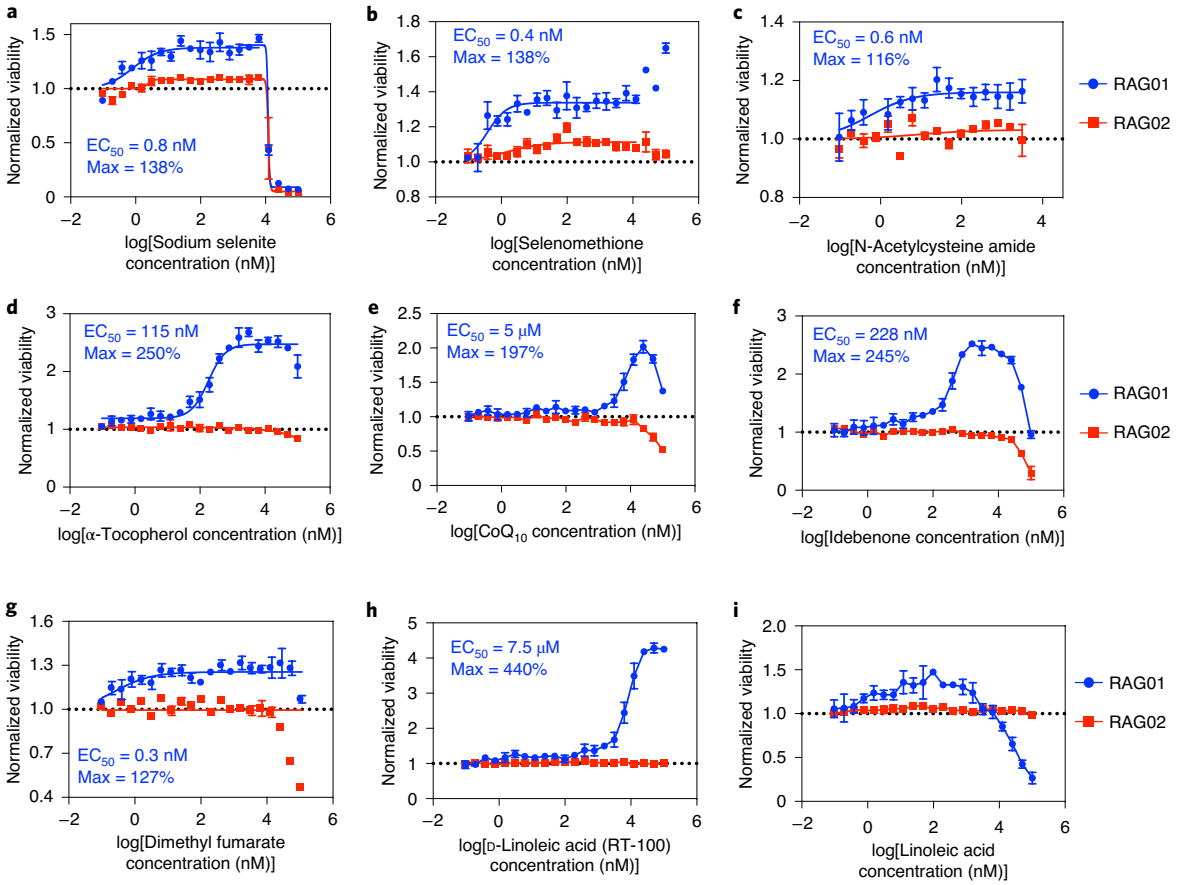

Fig. 6 | Proof-of-concept treatments on patient fibroblast. Supplements of sodium selenite (**a**), selenomethione (**b**), *N*-acetylcysteine amide (**c**), α-tocopherol (**d**), CoQ_{10} (**e**), idebenone (**f**), dimethyl fumarate (**g**), D-linoleic acid (**h**) and linoleic acid (**i**) were tested as proof-of-concept treatments on the patient and control fibroblasts. α-Tocopherol was removed from the medium in advance and fibroblast cells were treated with proof-of-concept treatments on day 5 without α-tocopherol. The increase in cell number was monitored compared with control fibroblast cells treated with dimethylsulfoxide only. Data are plotted as means ± s.d. ($n = 3$ biologically independent samples).

selenomethione and methylselenocysteine might be preferred owing to their lack of toxicity. It was also noteworthy that the rescue effect of selenium was specific for RAG01, with relatively minimal effect on the control RAG02 line.

Moreover, we included *N*-acetylcysteine and *N*-acetylcysteine amide in the test as metabolic precursors for the GPX4 cofactor GSH, which might also benefit patients[22]. We found that *N*-acetylcysteine and *N*-acetylcysteine amide could boost the viability of RAG01 cells slightly to 118% and 116%, which was less effective than selenocysteine (Fig. 6c and Extended Data Fig. 9b). This suggests the utility of selenium for patients with compromised GPX4 activity, and that elevation of GSH in cells might be helpful in boosting the activity of GPX4.

In addition, we evaluated the lipophilic antioxidants α-tocopherol, CoQ_{10} and idebenone (a soluble analog of CoQ_{10}), and found that they can also boost the viability of RAG01 cells to 250%, 197% and 245%, with EC_{50} values of 115 nM, 5 μM and 228 nM, respectively (Fig. 6d–f). We also found that dimethyl fumarate, an Nrf2 (nuclear factor erythroid 2-related factor 2) activator that promotes an antioxidant response, boosted the viability of RAG01 slightly to 127% (Fig. 6g)[23]. These results suggest that lipophilic antioxidant supplements, and possibly dimethyl fumarate to a limited extent, may be useful for patients with the R152H GPX4 variant.

Finally, we found that treatment with deuterium-reinforced linoleic acid (RT-001), a polyunsaturated fatty acid with deuterium at its bis-allylic site to inhibit lipid peroxidation, had the most pronounced rescue effect on RAG01 (440%, Fig. 6h)[18,24–26]. By contrast, normal linoleic acid was toxic to RAG01 at high concentrations, which suggested the likely involvement of lipid peroxidation in the compromised cell viability observed on patient cells (Fig. 6i).

To further evaluate the potency of the proof-of-concept treatments and compare their effects on $GPX4^{R152H}$ with a control expressing WT GPX4 (instead of RAG02 expressing both wild-type and the variant), we tested all treatments on Gpx4-knockout Pfa1 cells that were transfected to overexpress human/murine $GPX4^{WT}$ or $GPX4^{R152H}$ (Extended Data Figs. 9c and 10). Ferrostatin-1, a radical-trapping inhibitor of lipid peroxidation and ferroptosis, was also included in this test; its substantial and selective rescue effect on cells solely expressing $GPX4^{R152H}$ demonstrated the involvement of lipid peroxidation and possibly ferroptosis in R152H GPX4 pathology. Proof-of-concept treatments effective on patient fibroblasts also showed consistent rescue effects on the Pfa1 cells, especially for α-tocopherol, CoQ_{10}, idebenone and RT-001.

In summary, the observation that selenium supplementation, ferroptosis inhibitors and antioxidants can increase the number and viability of patient fibroblasts and R152H GPX4 cell models were consistent with the conclusion that the partial loss-of-function R152H mutation in GPX4 sensitizes patient cells to lipid peroxidation. Therefore, we expect that a combination treatment of selenium supplementation to boost R152H GPX4 levels and lipophilic antioxidants (α-tocopherol and/or CoQ_{10}) with deuterated polyunsaturated fatty acids such as RT-001, some of which are widely

available as supplements, to suppress lipid peroxidation might be the most effective treatment and may be therapeutically beneficial for patients with the R152H variant in GPX4.

Discussion

Before this study, patients with SSMD were identified as having predicted loss-of-function variants based on in silico data alone; the variants were not studied experimentally[3,4]. Our report provided evidence of the association of biallelic variants in GPX4 with SSMD. In addition, this report extends the phenotype associated with SSMD to include long-term survival beyond infancy.

This study began by examining the effect of the R152H missense mutation on GPX4, which adversely changed the protein structure and caused a partial loss of antioxidant activity. We hypothesize that, as a hypomorphic allele, there is sufficient enzymatic function to allow for survival beyond infancy, but with impaired proliferation and increased susceptibility to lipid peroxidation, ferroptosis, tissue damage and degeneration. This is in keeping with observations of the adult conditional Gpx4-knockout mouse, which exhibits perinatal lethality, seizures, ataxia and progressive neuronal loss[7,27,28].

During our analysis, we used structure-based computational modeling to study the effect of the variant on protein structure in silico, predictions from which were confirmed by protein crystal structures and cellular assays. These experiments suggested the feasibility of structure-based modeling of variant protein structures to dissect the impact of patient-derived variants. The low cost and high throughput of computational modeling would potentially benefit more patients with orphan diseases or variation in key genes.

This R152H variant unexpectedly revealed the structural basis of GPX4's enzymatic activity and regulation of its degradation: Lys48 was found to modulate GPX4 enzymatic activity and Lys125/Lys127 were revealed as sites of ubiquitin ligation. In addition, our study of R152H suggested Arg152 as an allosteric site indirectly regulating GPX4 activity. Because recent studies highlighted GPX4 protein as an Achilles heel of drug-resistant and metastatic cancers, which are exceptionally dependent on the GPX4 lipid peroxide repair pathway, we would expect biochemical therapeutic strategies targeting the essential residue Lys48 and allosteric site Arg152, or taking advantage of its degradation mechanism, to be developed as a high priority and benefit additional patients[29–31].

Online content

Any methods, additional references, Nature Research reporting summaries, source data, extended data, supplementary information, acknowledgements, peer review information; details of author contributions and competing interests; and statements of data and code availability are available at https://doi.org/10.1038/s41589-021-00915-2.

Received: 9 April 2021; Accepted: 1 October 2021;
Published online: 20 December 2021

References

1. Elcioglu, N. & Hall, C. M. Spondylometaphyseal dysplasia-Sedaghatian type. *Am. J. Med. Genet.* **76**, 410–414 (1998).
2. İpek, M. S. & Akin, A. Sedaghatian-type spondylometaphyseal dysplasia: a case of rapid demise with evidence of myocardial injury. *J. Genet. Genome Res.* **3**, 25–27 (2016).
3. Smith, A. C. et al. Mutations in the enzyme glutathione peroxidase 4 cause Sedaghatian-type spondylometaphyseal dysplasia. *J. Med. Genet.* **51**, 470–474 (2014).
4. Fedida, A. et al. Sedaghatian-type spondylometaphyseal dysplasia: whole exome sequencing in neonatal dry blood spots enabled identification of a novel variant in GPX4. *Eur. J. Med. Genet.* **63**, 104020 (2020).
5. Brigelius-Flohe, R. & Maiorino, M. Glutathione peroxidases. *Biochim. Biophys. Acta* **1830**, 3289–3303 (2013).
6. Yang, W. S. et al. Regulation of ferroptotic cancer cell death by GPX4. *Cell* **156**, 317–331 (2014).
7. Seiler, A. et al. Glutathione peroxidase 4 senses and translates oxidative stress into 12/15-lipoxygenase dependent- and AIF-mediated cell death. *Cell Metab.* **8**, 237–248 (2008).
8. Yant, L. J. et al. The selenoprotein GPX4 is essential for mouse development and protects from radiation and oxidative damage insults. *Free Radic. Biol. Med.* **34**, 496–502 (2003).
9. Tosatto, S. C. et al. The catalytic site of glutathione peroxidases. *Antioxid. Redox Signal.* **10**, 1515–1526 (2008).
10. Roveri, A., Maiorino, M. & Ursini, F. Enzymatic and immunological measurements of soluble and membrane-bound phospholipid–hydroperoxide glutathione peroxidase. *Methods Enzymol.* **233**, 202–212 (1994).
11. Ingold, I. et al. Selenium utilization by GPX4 is required to prevent hydroperoxide-induced ferroptosis. *Cell* **172**, 409–422 e421 (2018).
12. Ingold, I. et al. Expression of a catalytically inactive mutant form of glutathione peroxidase 4 (Gpx4) confers a dominant-negative effect in male fertility. *J. Biol. Chem.* **290**, 14668–14678 (2015).
13. Mannes, A. M., Seiler, A., Bosello, V., Maiorino, M. & Conrad, M. Cysteine mutant of mammalian GPx4 rescues cell death induced by disruption of the wild-type selenoenzyme. *FASEB J.* **25**, 2135–2144 (2011).
14. Borchert, A. et al. Crystal structure and functional characterization of selenocysteine-containing glutathione peroxidase 4 suggests an alternative mechanism of peroxide reduction. *Biochim. Biophys. Acta Mol. Cell. Biol. Lipids* **1863**, 1095–1107 (2018).
15. Zhu, K. et al. Docking covalent inhibitors: a parameter free approach to pose prediction and scoring. *J. Chem. Inf. Model.* **54**, 1932–1940 (2014).
16. Mauri, P. et al. Versatility of selenium catalysis in PHGPx unraveled by LC/ESI-MS/MS. *Biol. Chem.* **384**, 575–588 (2003).
17. Shimada, K. et al. Global survey of cell death mechanisms reveals metabolic regulation of ferroptosis. *Nat. Chem. Biol.* **12**, 497–503 (2016).
18. Gaschler, M. M. et al. FINO2 initiates ferroptosis through GPX4 inactivation and iron oxidation. *Nat. Chem. Biol.* **14**, 507–515 (2018).
19. Wu, Z. et al. Chaperone-mediated autophagy is involved in the execution of ferroptosis. *Proc. Natl Acad. Sci. USA* **116**, 2996–3005 (2019).
20. Romanowska, M. et al. Effects of selenium supplementation on expression of glutathione peroxidase isoforms in cultured human lung adenocarcinoma cell lines. *Lung Cancer* **55**, 35–42 (2007).
21. Bodnar, M., Szczyglowska, M., Konieczka, P. & Namiesnik, J. Methods of selenium supplementation: bioavailability and determination of selenium compounds. *Crit. Rev. Food Sci. Nutr.* **56**, 36–55 (2016).
22. Yang, W. S. & Stockwell, B. R. Ferroptosis: death by lipid peroxidation. *Trends Cell Biol.* **26**, 165–176 (2016).
23. Wang, Q. et al. Dimethyl fumarate protects neural stem/progenitor cells and neurons from oxidative damage through Nrf2-ERK1/2 MAPK pathway. *Int. J. Mol. Sci.* **16**, 13885–13907 (2015).
24. Hatami, A. et al. Deuterium-reinforced linoleic acid lowers lipid peroxidation and mitigates cognitive impairment in the Q140 knock in mouse model of Huntington's disease. *FEBS J.* **285**, 3002–3012 (2018).
25. Yang, W. S. et al. Peroxidation of polyunsaturated fatty acids by lipoxygenases drives ferroptosis. *Proc. Natl Acad. Sci. USA* **113**, E4966–E4975 (2016).
26. Brenna, J. T. et al. Plasma and red blood cell membrane accretion and pharmacokinetics of RT001 (bis-allylic 11,11-D2-linoleic acid ethyl ester) during long term dosing in patients. *J. Pharm. Sci.* **109**, 3496–3503 (2020).
27. Yoo, S. E. et al. Gpx4 ablation in adult mice results in a lethal phenotype accompanied by neuronal loss in brain. *Free Radic. Biol. Med.* **52**, 1820–1827 (2012).
28. Wirth, E. K. et al. Neuronal selenoprotein expression is required for interneuron development and prevents seizures and neurodegeneration. *FASEB J.* **24**, 844–852 (2010).
29. Hangauer, M. J. et al. Drug-tolerant persister cancer cells are vulnerable to GPX4 inhibition. *Nature* **551**, 247–250 (2017).
30. Liu, H., Schreiber, S. L. & Stockwell, B. R. Targeting dependency on the GPX4 lipid peroxide repair pathway for cancer therapy. *Biochemistry* **57**, 2059–2060 (2018).
31. Viswanathan, V. S. et al. Dependency of a therapy-resistant state of cancer cells on a lipid peroxidase pathway. *Nature* **547**, 453–457 (2017).

Methods

Patient cohorts. In this study, we identified three individuals with SSMD features who were found to harbor a recurrent homozygous R152H point mutation in the *GPX4* gene.

At 5 months of age, patient 1 (family 1) was diagnosed on brain auditory-evoked responses testing to have neurosensory hearing loss. The metabolic bone clinic suggested metaphyseal dysplasia. Whole-exome sequencing of patient 1 and his parent was conducted. Only one gene variant was identified, c.455G>A (p. R152H) of *GPX4*, which was found to segregate in each parent and presented in the patient as a homozygous biallelic variant.

A skeletal survey of patient 2 (family 2) at 7 years of age revealed flaring of the proximal tibial metaphysis as well as distal femoral metaphysis, brachycephaly, moderate thoracolumbar levoscoliosis, coxa valga, thin and elongated second metatarsals and diffuse osteopenia with thinning of the long bones. Patient 3 (family 2) is the younger sister of patient 2. Patient 3 did not pass her newborn hearing screen and subsequent brainstem auditory-evoked response testing revealed bilateral auditory neuropathy. Whole-exome sequencing was also obtained clinically on family 2, and reported the same variant in *GPX4* as family 1.

See Supplementary Note for clinical observations of the three patients. All three patients and their families (patient 1 from family 1, and patients 2 and 3 from family 2) gave informed consent for genetic and clinical investigation. Both families were enrolled in an institutional approved study of children with undiagnosed neurogenetic disorders (Genomic Sequencing in Neurological Disorders research protocol, UCSD IRB #170437). Tissue sampling (including skin biopsy for the development of fibroblasts RAG01 and RAG02) and clinical observations of patient 1 and his parent were approved by IRB #00002259 (Molecular and Biochemical Analysis of Metabolic Disorders, University of Washington). Study of GPX4 variant in the human fibroblast samples was approved by IRB #AAAS9249 (Evaluation of GPX4 variant activity in fibroblasts, Columbia University). Compensation was not provided.

Whole-exome sequencing. Whole-exome sequencing of all three patients was performed at GeneDx. Ages at sequencing were 9 months for patient 1 (male, May 2019), 7 years for patient 2 (male, December 2015) and 10 months for patient 3 (female, December 2015). An Agilent clinical research exome kit was used for DNA fragment capture. NextGen sequencing (massive parallel sequencing) was performed on a HiSeq platform (Illumina). Exome GRCh37/hg19 was used as the reference in the custom analysis tool Xome Analysis to detect the patient-derived variant. Whole-exome sequencing results are summarized in Supplementary Table 1.

Cell lines. HT-1080 cells were obtained from ATCC and grown in DMEM with glutamine and sodium pyruvate (Corning 10-013) supplemented with 10% fetal bovine serum (FBS), 1% nonessential amino acids (Invitrogen) and 1% penicillin–streptomycin mix (Invitrogen). Tam-inducible *Gpx4*$^{-/-}$ murine embryonic fibroblasts (Pfa1) were used as described previously[7,11–13]. *Gpx4*$^{-/-}$ Pfa1 cells were grown in DMEM supplemented with 10% FBS, 1% glutamine, 1% penicillin–streptomycin mix, 750 μg ml^{-1} neomycin, 1 μM puromycin and 1 μM tamoxifen. *Gpx4*$^{-/-}$ HT1080 cells were grown in DMEM supplemented with 10% FBS, 1% glutamine, 1% penicillin–streptomycin mix, 750 μg ml^{-1} neomycin. We found that *Gpx4*-knockout cells solely expressing GPX4^{R152H}, similar to *Gpx4*-knockout cells, required α-tocopherol for normal growth. Therefore, α-tocopherol was supplemented in the culture media of *Gpx4*-knockout cells solely expressing GPX4^{R152H}. However, it is noteworthy that overoxidation and deactivation of R152H GPX4 by lipid peroxides would be artificially masked by the lipophilic antioxidant α-tocopherol, which may directly reduce the oxidized form of the GPX4 active site (selenenic or seleninic form), as demonstrated by the slightly higher activity of R152H GPX4 in cells cultured in medium with α-tocopherol (Fig. 2c).

Human fibroblast cell lines RAG01 and RAG02 were developed from the patient with the homozygous R152H variant and his parent heterozygous for the R152H variant. At the time of sample collection, the patient (male, RAG01) was 22 months old, and his parent (male, RAG02) was 31 years old. RAG01 and RAG02 were grown in DMEM with glutamine and sodium pyruvate (Corning 10-013) supplemented with 15% FBS, 1% nonessential amino acids (Invitrogen), 1% penicillin–streptomycin mix (Invitrogen). Similar to *Gpx4*-knockout cells overexpressing R152H GPX4, patient fibroblast cells, RAG01, also required α-tocopherol for normal growth at low seeding densities; thus, α-tocopherol (10 μM) was supplemented in the medium for fibroblast cell lines and was only removed in advance of testing cellular viabilities. It is noteworthy that although the loss of GPX4 activity caused by R152H in fibroblasts appeared to be to a lesser extent than observed in the previous cell models, this might be because the control line RAG02 also expressed R152H GPX4, and also because fibroblast cells were cultured in medium supplemented with α-tocopherol, which was able to artificially mask the deactivation of R152H GPX4 by lipid peroxides (Fig. 5b). RAG01 and RAG02 cell lines are available for both commercial and academic use through CureGPX4.org, a patient organization dedicated to finding a treatment for SSMD disease.

Cells were maintained in a humidified environment at 37 °C and 5% CO_2 in a tissue incubator.

Computational modeling and molecular dynamics simulation. In silico residue mutation analysis, MD simulations and ligand docking were performed in Maestro (Schrödinger Suite). Because all variants of the GPX4 protein that we physically purified in vitro (GPX4^{R152H}, GPX4^{K48A} and GPX4^{K48L}) have the U46C mutation to aid protein expression, we started from computational modeling on GPX4 with the U46C mutation in silico either to directly compare our crystal structures for the GPX4 protein (GPX4^{R152H}) and the computationally predicted GPX4^{R152H} structure side-by-side, or to use our crystal structures of GPX4 protein (GPX4^{K48A} and GPX4^{K48L}) as starting points for MD simulations. We then performed computations on GPX4^{WT} structure (PDB: 6HN3) as a confirmatory control to rule out the possibility of artificial effects caused by the U46C mutation. Eventually, consistent results were observed, regardless of whether GPX4^{U46C} or GPX4^{WT} was used as the input.

To model the structure of GPX4^{R152H}, and the crystal structures of GPX4^{U46C} (PDB: 2OBI) and GPX4^{WT} (PDB: 6HN3) were imported into Maestro, preprocessed to remove water and add hydrogens, optimized at pH 7 for H-bond assignment and minimized in the OPLS3e force field using Protein Preparation Wizard. Substitution of the Arg152 residue in the structure by His was followed by global minimization of the whole structure in an implicit solvent to generate the R152H model. As a control, GPX4^{R152R} was also generated by synonymous mutation of Arg152 to Arg using the same algorithm and minimization method to rule out the possibility of artificial effects caused by the computation process. For models that featured the U46C mutation, the cysteine thiol of C46 was manually set to a thiolate anion to mimic the active form of the enzyme because the selenocysteine has a lower pK_a value and would convert to the anion form under physiological conditions. SiteMap was then run under the default setting. A structural comparison of GPX4^{R152H} and GPX4^{R152R} was performed thereafter.

To further study the impact of R152H mutation with MD simulation, each of the above modeled structures was set up in an orthorhombic box with 0.15 M NaCl in simple point-charge (SPC) water and an OPLS3e force field, unless noted otherwise. Multiple independent MD simulations of each system for 100 ns with 4.8 ps per step at 300 K and 1.01325 bar were performed with random seeding in Desmond Molecular Dynamics. Trajectories were recorded and analyzed. Simulation quality and event analysis were also performed using Desmond. Videos of representative simulation processes were exported.

It is noteworthy that the GPX4^{R152H} crystal structure that we solved (PDB: 7L8L) was not used for MD simulation because the loop between P124 and A133 does not exhibit a defined structure, which would complicate the modeling. It is also noteworthy that a previously published crystal structure of GPX4^{U46C} (PDB: 2OBI) was used above to model the GPX4^{R152H} structure. This is because this modeling was done before all other experiments in a wet lab, including acquisition of our own crystal structure of GPX4^{U46C} (PDB: 7L8K). Later, we found that the structure of GPX4^{U46C} (PDB: 7L8K) we solved is consistent with the previously reported structure (PDB: 2OBI). We then used 7L8K for all the following computational work.

To study the impact of K48 mutations on reduced GPX4, the GPX4^{U46C} (PDB: 7L8K), GPX4^{U46C_K48A} (PDB: 7L8R) and GPX4^{U46C_K48L} (PDB: 7L8M) crystal structures that we solved were respectively set up in an orthorhombic box and analyzed with MD simulations using the same protocol as noted above. Additional K48 variants modeled from GPX4^{WT} were also analyzed in the same protocol.

To study the impact of K48 mutations on oxidized GPX4, the fully oxidized GPX4^{U46C} crystal structure (PDB: 7L8Q) that we solved was not used for MD simulation. Instead, for side-by-side comparison, we manually set the cysteine thiol of C46 in GPX4^{U46C} (PDB: 7L8K), GPX4^{U46C_K48A} (PDB: 7L8R) and GPX4^{U46C_K48L} (PDB: 7L8M) to be fully oxidized. After confirmation of the relevance of the modeled oxidized structure by comparing it with the crystal structure, we used these fully oxidized structures in the MD simulation, as described above.

In addition, covalent docking of GSH was performed on the crystal structures of GPX4^{U46C} (PDB: 7L8K), GPX4^{U46C_K48A} (PDB: 7L8R) and GPX4^{U46C_K48L} (PDB: 7L8M), which were solved and reported in this work. Other docking receptors of GSH are the crystal structure of GPX4^{WT} (PDB: 6HN3) and modeled structures based on it.

Generation of HT-1080 cells expressing tagged GPX4. A pBabe-puro (pBP) vector incorporated into the complementary DNA of GFP-tagged cyto-GPX4^{WT} was prepared in a previous study (pBP–GFP–cGPX4^{WT})[6]. With the vector as a template, the following mutagenesis primers were designed using the Agilent QuikChange Primer Design application: R152H (5'-CTGCGTGGTGAAGC ACTACGGACCCATGG-3', 5'-CCATGGGTCCGTAGTGCTTCACCACGCAG -3'), K48A (5'-GGCCTCCCAGTGAGGCGCGACCGAAGTAAACTAC-3', 5'-GTAGTTTACTTCGGTCGCGCCTCACTGGGAGGCC-3'), K125R_K127R (5'-TGGATGAAGATCCAACCCAGGGGCAGGGGCATCCTG-3', 5'-CAGGATG CCCCTGCCCCTGGGTTGGATCTTCATCCA-3'). Primers were purchased from Integrated DNA Technologies. A site-directed mutagenesis kit (QuikChange II, Agilent 200521) was then used to acquire pBP–GFP–cGPX4^{R152H}, pBP–GFP–cGPX4^{K48A} and pBP–GFP–cGPX4^{K125R_K127R}. K48L mutation was conducted by GENEWIZ mutagenesis service on the same template vector to acquire pBP–GFP–cGPX4^{K48L}. All resulting plasmids were confirmed by sequencing at GENEWIZ.

HT-1080 cells were seeded in a six-well dish at a density of 300,000 cells per well the night before lipofection. Some 2.5 μg of DNA (empty pBP vector and the above five GFP–GPX4 expressing pBP vectors, separately), 7.5 μl of Lipofectamine

3000 (Invitrogen, catalog number L3000015) and 250 µl of Opti-MEM were incubated for 5 min at room temperature before adding to the HT1080 cells. Following transfection, cells were passaged several times in HT1080 media containing 1.5 mg ml^{-1} puromycin and grown in this media for all experiments. Expression of the exogenous GFP-tagged GPX4 was confirmed with a fluorescence microscope and western blotting with both GFP and GPX4 antibodies.

Western blot. For quantification of the cellular GPX4 protein level for the GPX4-specific activity assay, biological duplicates of each cell line subject to the GPX4-specific activity were tested by western blotting in technical duplicates, giving a total of four samples for each cell line. In particular, cells were harvested with trypsin (Invitrogen, catalog number 25200-114), pelleted and lysed with LCW lysis buffer (0.5% Triton X-100, 0.5% sodium deoxycholate salt, 150 mM NaCl, 20 mM Tris–HCl, pH 7.5, 10 mM EDTA, 30 mM Na-pyrophosphate and cOmplete protease inhibitor cocktail). One part of the cell lysates was blotted for protein quantification and the other part was used for the GPX4-specific activity assay.

For the GPX4 degradation study, cells were seeded at 800,000 per well in a 60-mm plate and allowed to adhere overnight. Cells were then treated with 100 µM α-tocopherol and either 1 µM RSL3, 1 µM ML162, 10 µM IKE, 10 µM FIN56 or vehicle for 10 h before harvest. Particularly for cycloheximide-chase analysis, cells were treated with 4 µM RSL3, 30 µg ml^{-1} cycloheximide and 100 µM α-tocopherol for 0, 2, 4 or 6 h before harvest. Each condition was performed at least twice. Cells were harvested with trypsin (Invitrogen, catalog number 25200-114), pelleted and lysed with RIPA buffer.

For both experiments, western blotting of each condition or cell line was performed at least twice. Cell lysates were blotted and imaged as previously described[6]. Antibodies used were GPX4 (Abcam, catalog number ab125066; 1:250 dilution), GFP (Santa Cruz, catalog number sc-9996; 1:10,00 dilution), actin (Cell Signaling, catalog number D18C11; 1:3,000 dilution), GAPDH (Santa Cruz, catalog number sc-47724; 1:10,000 dilution), IRDye 800CW goat anti-rabbit IgG secondary antibody (LI-COR, catalog number 926-33221; 1:5,000) and goat anti-mouse IgG (H+L) secondary antibody conjugated with AlexaFluor 680 (ThermoFisher Scientific, catalog number A-21057; 1:5,000). Results were quantified using a LI-COR Odyssey CLx IR scanner and ImageJ, and plotted using GraphPad Prism.

Determination of GPX4-specific activity. We applied a NADPH-coupled cellular GPX4 enzymatic activity assay, as previously reported[10]. Oxidized glutathione, generated by GPX4 during reduction of its specific phospholipid hydroperoxides substrate, was reduced by glutathione reductase at the expense of NADPH, and the decrease in the characteristic absorbance at 340 nm was monitored and quantified as GPX4 activity. The GPX4-specific substrate phosphatidylcholine hydroperoxide (PCOOH) was prepared by enzymatic hydroperoxidation of phosphatidylcholine by soybean lipoxidase type IV: 22 ml of 0.2 M Tris–HCl, pH 8.8, containing 3 mM sodium deoxycholate and 0.3 mM phosphatidylcholine was incubated at room temperature, under continuous stirring for 30 min with 0.7 mg of soybean lipoxidase type IV. The mixture was loaded onto a Sep-Pak C18 cartridge (Waters-Millipore) washed with methanol and equilibrated with water. After washing with 10 volumes of water, phosphatidylcholine hydroperoxides were eluted in 2 ml of methanol.

To measure the GPX4 activity for specific cell lines of interest, 48 million cells of each cell line were harvested and lysed using LCW lysis buffer. The concentration of protein in the lysate was determined using a bicinchoninic acid (BCA) assay kit with BSA as standard. Then, on a 96-well plate, 250 µl of 1.5 µg ml^{-1} cell lysate was incubated in GPX4 activity assay buffer (0.1% Triton X-100, 100 mM Tris–HCl, pH 7.4, 10 mM NaN_3, 5 mM EDTA, 0.6 IU ml^{-1} glutathione reductase, 0.5 mM NADPH) at 37 °C for 10 min. PCOOH was then added to the mixture to initiate GPX4 reaction. The absorbance of NADPH at 340 nm was determined kinetically at 1-min intervals over 20 min. GPX4 activity was calculated based on the assumption rate of NADPH during this kinetic process. Experiments using lysis buffer instead of cell lysate and controls without addition of PCOOH were also carried out to measure the particular activity of GPX4 to reduce phospholipid hydroperoxides. The total GPX4 activity of each sample was normalized to its specific GPX4 level based on western blotting for unit GPX4 enzymatic activity for comparison. Results were quantified using GraphPad Prism v.9.

To measure the effect of small molecules on GPX4 enzymatic activity, 3 µl of 10 mM compound or dimethylsulfoxide control were added to the 96-well plate first, before addition of 147 µl of 1.5 µg ml^{-1} cell lysate in the GPX4 activity assay buffer and sequential incubation at 37 °C for 20 min. PCOOH was then added to the mixture to initiate GPX4 reaction and the GPX4 activity was measured as above.

Cellular viability assay. To monitor the viability of cells without α-tocopherol supplementation, cells that had been cultured in media with and without α-tocopherol supplementation were harvested with trypsin, pelleted, washed three times with PBS, counted by Vi-cell (Beckman), partially collected for the GPX4-specific activity assay and then equivalently seeded into new cell culture flasks in media without α-tocopherol supplementation on day 1. Every other day (day 3, 5 and 7), cells were harvested with trypsin, counted by Vi-cell, partially collected for the GPX4-specific activity assay, before seeding back equivalent number of cells in the corresponding flasks. For quantification, viability was based on normalization of the viable cell number for each cell line to the total cell number of the corresponding cell line expressing WT GPX4.

For dose–response curves, cells were harvested with trypsin, pelleted and counted by Vi-cell before seeding into plates. One thousand cells were plated at 36 µl per well of a 384-well plate on day 1. For cell lines that were also subjected to the GPX4-specific activity, the remaining cells (after seeding into plates) were immediately tested by western blotting and the activity assay described above. Compounds were dissolved in dimethylsulfoxide and a twofold dilution series was prepared. The compounds were then diluted 1:50 in media and 4 µl was added to each well of the plates on day 2. After 48 h of treatment, the viability of cells was measured using a 1:1 dilution of CellTiter-Glo luminescent reagent (Promega, catalog number G7573) with media, which was read on a Victor 5 plate reader after 10 min of shaking at room temperature on day 4. The intensity of the luminescence was normalized to that of the dimethylsulfoxide control. Results were quantified using GraphPad Prism v.9.

Protein purification. GPX4 is a selenoprotein with selenocysteine at its active site (U46). Large-scale expression of selenocysteine-containing proteins in recombinant systems is challenging because of inefficient selenocysteine-incorporating machinery; thus, the selenocysteine to cysteine (U to C, inserting a thiol group in place of the selenol group) mutant of GPX4 is widely used in structural studies, despite its lower enzymatic activity compared with the WT protein[32–35]. Because recent studies on selenocysteine-containing GPX4 confirmed the relevance of the catalytic tetrad and other structural properties discovered in the context of the U to C mutant, we used a GPX4^{U46C} construct for in vitro structural studies, and simultaneously examined the selenocysteine-containing cytosolic GPX4 in structure-based computational analysis and human cells via enzymatic assays and cellular assays[11,14,36].

The bacterial expression vector pOE30-His-tagged-c-GPX4^{U46C} has been described previously[25]. With the vector as a template, the following mutagenesis primers were designed using the Agilent QuikChange Primer Design application: R152H (forward: 5'-CTGCGTGGTGAAGCACTACGGACCCATGG-3', reverse: 5'-CCATGGGTCCGTAGTGCTTCACCACGCAG-3'), K48A (forward: 5'-GGCCTCCCAGTGTGGCGCGACCGAAGTAAACTAC-3', reverse: 5'-GTAGTTTACTTCGGTCGCGCCACACTGGGAGGCC-3'), K48L (forward: 5'-CGTGGCCTCCCAGTGTGGCCTAACCGAAGTAAACTACACTC-3', reverse: 5'-GAGTGTAGTTTACTTCGGTTAGGCCACACTGGGAGGCCACG-3'). Primers were purchased from Integrated DNA Technologies. A site-directed mutagenesis kit (QuikChange II, Agilent, catalog number 200521) was then used to acquire pOE30–c-GPX4^{U46C_R152H}, pOE30–c-GPX4^{U46C_K48A} and pOE30–c-GPX4^{U46C_K48L}. All mutations and the resulting plasmids were confirmed by sequencing at GENEWIZ.

Isolated colonies with each plasmid were separately transferred to 8 ml of Luria–Bertani (LB) medium with 100 µg ml^{-1} ampicillin, and the inoculated culture was incubated with shaking (225 r.p.m.) at 37 °C for 16 h. Three milliliters of starter culture was added to 1 l of fresh LB medium with 100 µg ml^{-1} ampicillin. The culture was incubated with shaking (225 r.p.m.) at 37 °C until the optical denisity at 600 nm reached 0.9. The temperature was then decreased to 15 °C. Cells were incubated overnight with 1 mM isopropyl-β-D-thiogalactoside at 15 °C while being shaken at 225 r.p.m. The next day, the bacteria were harvested by centrifugation at 4,000*g* for 20 min at 4 °C and the pellet obtained was used for purification or stored at −20 °C. The pellet was resuspended in 25 ml of chilled lysis buffer (100 mM Tris, pH 8.0, 300 mM NaCl, 20 mM imidazole, 3 mM tris(2-carboxyethyl) phosphine (TCEP) and Roche protease inhibitor cocktail). Bacteria were lysed by sonication on ice for 6 min, and the lysate was centrifuged at 10,000 r.p.m. for 20 min at 4 °C to remove cell debris. The clarified lysate was incubated with Ni Sepharose 6 Fast Flow beads (GE Life Sciences) on a rotator at 4 °C for at least 1 h. The beads were washed with wash buffer (100 mM Tris, pH 8.0, 300 mM NaCl, 50 mM imidazole and 3 mM TCEP) to remove nonspecific binding. The protein was eluted with 100 mM Tris, pH 8.0, 300 mM NaCl, 100 mM imidazole and 3 mM TCEP. The protein was further purified using a gel filtration Superdex 200 column in fast protein liquid chromatography (FPLC) buffer containing 100 mM Tris, pH 8.0, 300 mM NaCl and 3 mM TCEP. Fractions containing GPX4 were pooled and analyzed by SDS–polyacrylamide gel electrophoresis.

Crystallization and structure determination. Protein samples of GPX4^{U46C} were initially screened at the High-Throughput Crystallization Screening Center[37] of the Hauptman-Woodward Medical Research Institute (HWI) (https://hwi.buffalo.edu/high-throughput-crystallization-center/). The most promising crystal hits were reproduced using an under oil micro batch method in a COY anaerobic glove box at 23 °C.

Plate-like crystals of GPX4^{U46C} were grown using a crystallization reagent comprising 0.056 M sodium phosphate monobasic monohydrate, pH 8.2, and 1.344 M potassium phosphate with a protein to crystallization reagent ratio of 2:1. All crystals were subsequently transferred into a similar crystallization reagent supplemented with 20% (v/v) glycerol and flash-frozen in liquid nitrogen in the glove box. A native dataset was collected on a crystal of GPX4^{U46C} at the

NE-CAT24-ID-C beam line of Advanced Photon Source in Lemont, IL, USA. Crystals of $GPX4^{U46C}$ were subsequently used as seeds for growing crystals of $GPX4^{U46C\_R152H}$, $GPX4^{U46C\_K48L}$, $GPX4^{U46C\_K48A}$ and $GPX4^{U46C}$-sulfone outside the glove box, albeit different crystallization conditions were used for growing these crystals. Crystals of $GPX4^{U46C\_R152H}$ were grown under crystallization conditions comprising 0.2 M sodium thiocyanate, pH 6.9, and 20% (w/v) polyethylene glycol (PEG) 8000, whereas crystals of K48L and K48A were grown under conditions of 0.1 M sodium chloride, 0.1 M MES, pH 6, and 40% (w/v) PEG 8000. Crystals of the fully oxidized $GPX4^{U46C}$-sulfone were grown in 0.1 M potassium thiocyanate, 0.1 M sodium acetate, pH 5, and 20% (w/v) PEG 8000, and were harvested after one month. In each case, crystals were transferred into the respective crystallization reagent, which was supplemented by 20% (v/v) ethylene glycol.

Crystals of $GPX4^{U46C}$, $GPX4^{U46C\_R152H}$, $GPX4^{U46C\_K48L}$, $GPX4^{U46C\_K48A}$ and $GPX4^{U46C}$-sulfone diffracted X-rays at a NE-CAT24-ID-C beam line to a resolution 1.38, 1.61, 2.07, 1.52 and 1.48 Å, respectively. The images were processed and scaled in space group $P2_1$, $P2_1$, $P2_1$, $P2_12_12_1$ and $P2_1$, using X-ray Detector Software (XDS)[38]. The structure of each protein was determined by molecular replacement using the MOLREP[39] program and the crystal structure of $GPX4^{U46C}$ (PDB: 2OBI) was used as a search model for structure determination of $GPX4^{U46C}$. The latter structure was used as the search model for subsequent structure determination of other crystal structures. The geometry of each crystal structure was fixed using programs XtalView[40] and COOT[41], and refined by Phenix[42]. There is one protomer of GPX4 in the asymmetric unit of the crystal with space group $P2_1$, whereas the asymmetric unit of $GPX4^{U46C\_K48A}$ with space group $P2_12_12_1$ contains two protomers. The crystallographic statistics is shown in Supplementary Table 4.

Thermal shift assay (determination of protein melt temperature). Because mutation of amino acid residues may alter the thermostability of a protein, we used a thermal shift assay to monitor the potential change in GPX4 thermostability caused by R152H mutation, which practically determined the change in the unfolding transition temperature (ΔT_m) obtained in the R152H mutant relative to that obtained in the wild-type[43,44]. We adapted the assay on a fast 96-well PCR plate. In vitro purified $GPX4^{U46C}$ or $GPX4^{U46C\_R152H}$ protein was diluted to 5 µM in 20 µl of fast protein liquid chromatography (FPLC) buffer (100 mM Tris, pH 8.0, 300 mM NaCl, 3 mM TCEP) in each well of a 96-well plate with 5× Sypro orange protein dye, which will bind to the hydrophobic patch of the protein once the protein is melted and then exhibit a stronger fluorescence signal. Multiple replicates were prepared for each protein variant. The thermal shift assay was performed on the ViiA 7 Real-Time PCR system (ThermoFisher Scientific) with the thermal protocol: 25 °C for 15 s, increase temperature to 99 °C at a rate of 0.05 °C s^{-1}, 99 °C for 15 s. Fluorescence was recorded and analyzed using Protein Thermal Shift software.

Immunofluorescence study and quantification. Human fibroblasts RAG01 and RAG02 were separately seeded on polylysine-coated coverslips (Sigma Aldrich, catalog number P4832) in a 24-well plate (100,000 cells per coverslip and three coverslips for each cell line) and allowed to grow overnight. Medium was removed and the cells were gently washed twice with PBS^{2+} (PBS with 1 mM $CaCl_2$ and 0.5 mM $MgCl_2$). The cells were fixed and permeabilized by adding 200 µl per well of 4% paraformaldehyde in PBS buffer with 0.1% Triton X-100 (PBS-T), and incubated at room temperature for 20 min. The cells were washed three times with PBS-T and blocked with 5% goat serum (ThermoFisher Scientific, catalog number 50197Z) in PBS-T for 1 h at room temperature. The cells were then incubated with monoclonal mouse GPX4 antibody (Santa Cruz, catalog number sc-166570; 1:500 dilution) in PBS-T with 1% BSA and 5% goat serum overnight at 4 °C, followed by washing three times with PB-T for 5 min each time. The cells were incubated with goat anti-mouse IgG (H+L) highly cross-adsorbed secondary antibody, AlexaFluor 594 (ThermoFisher Scientific, catalog number A-11032, RRID:AB_2534091; 1:200 dilution) at room temperature for 1 h and then washed with three times with PBS-T for 5 min each time. ProLong Diamond anti-fade mountant with DAPI (ThermoFisher Scientific, catalog number P36962) was added to stain the nucleus. All images were captured on a Zeiss LSM 800 confocal microscope at Plan-Apochromat ×63/1.40 oil differential interference contrast objective with constant laser intensity for all samples.

Quantification of the intensity of antibodies was analyzed using CellProfiler v.3.1.8 (ref. [45]) (CellProfiler Image Analysis Software, RRID:SCR_007358). Nuclei were first identified as primary objects using a global minimum cross entropy strategy, based on the DAPI fluorescence signal. Whole cells were then identified as secondary objects based on the primary objects by propagation using a global minimum cross entropy strategy, based on the GPX4 fluorescence (AlexaFluor 594) signal. The cytoplasm was identified as the tertiary object as the part of each cell excluding the nucleus. Mean intensities of GPX4 fluorescence of nuclei, cytoplasm and whole cells were measured and reported. Graphs were created in GraphPad Prism v.9.

Statistical analyses. All experiments, unless otherwise indicated, are biological replicates based on distinct samples. All statistical analyses were performed using GraphPad Prism v.9. Tukey's test was performed as a post-hoc test after ordinary one-way ANOVA, comparing all pairwise datasets, with alpha = 0.05. Sidak's test was performed as a post-hoc test after ordinary two-way ANOVA for grouped data, comparing pairwise datasets in each group. Only relevant pairwise comparisons are highlighted in the figures. Unpaired Student's *t*-test was performed when indicated in the manuscript, for comparing two experimental conditions. All *t*-tests were two-tailed with a significance threshold of $P < 0.05$.

Reporting Summary. Further information on research design is available in the Nature Research Reporting Summary linked to this article.

Data availability

Crystal structural coordinates were deposited in the RCSB, with accession codes PDB IDs: 7L8K, 7L8L, 7L8M, 7L8R, and 7L8Q. Publicly available datasets used in this study are: PDB IDs: 2OBI, 6HN3. Source data are provided with this paper.

References

32. Janowski, R., Scanu, S., Niessing, D. & Madl, T. Crystal and solution structural studies of mouse phospholipid hydroperoxide glutathione peroxidase 4. *Acta Crystallogr. F Struct. Biol. Commun.* **72**, 743–749 (2016).
33. Li, C. et al. Novel allosteric activators for ferroptosis regulator glutathione peroxidase 4. *J. Med. Chem.* **62**, 266–275 (2019).
34. Sakamoto, K. et al. Discovery of GPX4 inhibitory peptides from random peptide T7 phage display and subsequent structural analysis. *Biochem. Biophys. Res. Commun.* **482**, 195–201 (2017).
35. Scheerer, P. et al. Structural basis for catalytic activity and enzyme polymerization of phospholipid hydroperoxide glutathione peroxidase-4 (GPx4). *Biochemistry* **46**, 9041–9049 (2007).
36. Yu, Y. et al. Characterization and structural analysis of human selenium-dependent glutathione peroxidase 4 mutant expressed in *Escherichia coli*. *Free Radic. Biol. Med.* **71**, 332–338 (2014).
37. Luft, J. R. et al. A deliberate approach to screening for initial crystallization conditions of biological macromolecules. *J. Struct. Biol.* **142**, 170–179 (2003).
38. Kabsch, W. Integration, scaling, space-group assignment and post-refinement. *Acta Crystallogr. D Biol. Crystallogr.* **66**, 133–144 (2010).
39. Vagin, A. & Teplyakov, A. Molecular replacement with MOLREP. *Acta Crystallogr. D Biol. Crystallogr.* **66**, 22–25 (2010).
40. McRee, D. E. XtalView/Xfit-A versatile program for manipulating atomic coordinates and electron density. *J. Struct. Biol.* **125**, 156–165 (1999).
41. Emsley, P., Lohkamp, B., Scott, W. G. & Cowtan, K. Features and development of Coot. *Acta Crystallogr. D Biol. Crystallogr.* **66**, 486–501 (2010).
42. Adams, P. D. et al. PHENIX: a comprehensive Python-based system for macromolecular structure solution. *Acta Crystallogr. D Biol. Crystallogr.* **66**, 213–221 (2010).
43. Lo, M. C. et al. Evaluation of fluorescence-based thermal shift assays for hit identification in drug discovery. *Anal. Biochem.* **332**, 153–159 (2004).
44. Kaplan, A. et al. Small molecule-induced oxidation of protein disulfide isomerase is neuroprotective. *Proc. Natl Acad. Sci. USA* **112**, E2245–E2252 (2015).
45. Carpenter, A. E. et al. CellProfiler: image analysis software for identifying and quantifying cell phenotypes. *Genome Biol.* **7**, R100 (2006).
46. Cheff, D. M. et al. Development of therapies for rare genetic disorders of GPX4: roadmap and opportunities. *Orphanet J. Rare Dis.* **16**, 446 (2021).

Acknowledgements

This study was supported by P01CA87497 (B.R.S.), R35CA209896 (B.R.S.) and R61NS109407 (B.R.S.), and the BMBF VIP+ program NEUROPROTEKT (03VP04260), the Ministry of Science and Higher Education of the Russian Federation (075-15-2019-1933) and the European Research Council (ERC) under the European Union's Horizon 2020 research and innovation program (grant agreement No. GA 884754) (M.C.). We thank Q. Ran for calling to attention that three patients reported in this study shared the same homozygous variant. We are grateful to the patient with the R152H variant and the patient's parent for providing their fibroblasts for this study. We thank the staff of the High-Throughput Crystallization Screening Center of the Hauptman-Woodward Medical Research Institute for screening of crystallization conditions and the staff of the Advanced Photon Source at Argonne National Laboratory for assistance with data collection. We also thank curegpx4.org for supporting the study and patients with GPX4 variants, and the roadmap effort for GPX4 disorders[46].

Author contributions

B.R.S. conceived and implemented the project after discussions with R.S. The planning and design of experiments was performed by H.L., T.S., R.S., M.C. and B.R.S. Computational modeling was conducted by H.L., as were biophysical assays, biochemical assays and cellular experiments. H.L. and X.X. conducted protein purification. F.F. crystallized the proteins and collected diffraction data to solve the crystal structures. T.S. and M.C. prepared GPX4-knockout Pfa1 and HT1080 cells. R.S., K.W. and J.F. conducted clinical observations of the patients. M.S.S. provided deuterium-reinforced linoleic acid. H.L. and B.R.S. wrote the manuscript with input from all authors.

Competing interests

B.R.S. is an inventor on patents and patent applications related to GPX4 and ferroptosis, and is a consultant to and cofounder of Inzen Therapeutics and Nevrox Limited, and is a member of the Scientific Advisory Board of Weatherwax Biotechnologies Corporation, and a consultant to Akin Gump Strauss Hauer & Feld LLP. M.C. is an inventor of ferroptosis-related patents and cofounder and shareholder of ROSCUE Therapeutics GmbH. J.F. participates in clinical trials with Biogen (Angelman's syndrome) and J.F.'s spouse is Founder and Principal of Friedman Bioventure, which holds a variety of publicly traded and private biotechnology interests. M.S.S. is the Chief Scientific Officer of Retrotrope, Inc.

Additional information

Extended data is available for this paper at https://doi.org/10.1038/s41589-021-00915-2.

Supplementary information The online version contains supplementary material available at https://doi.org/10.1038/s41589-021-00915-2.

Correspondence and requests for materials should be addressed to Brent R. Stockwell.

Peer review information *Nature Chemical Biology* thanks Dohoon Kim and the other, anonymous, reviewer(s) for their contribution to the peer review of this work.

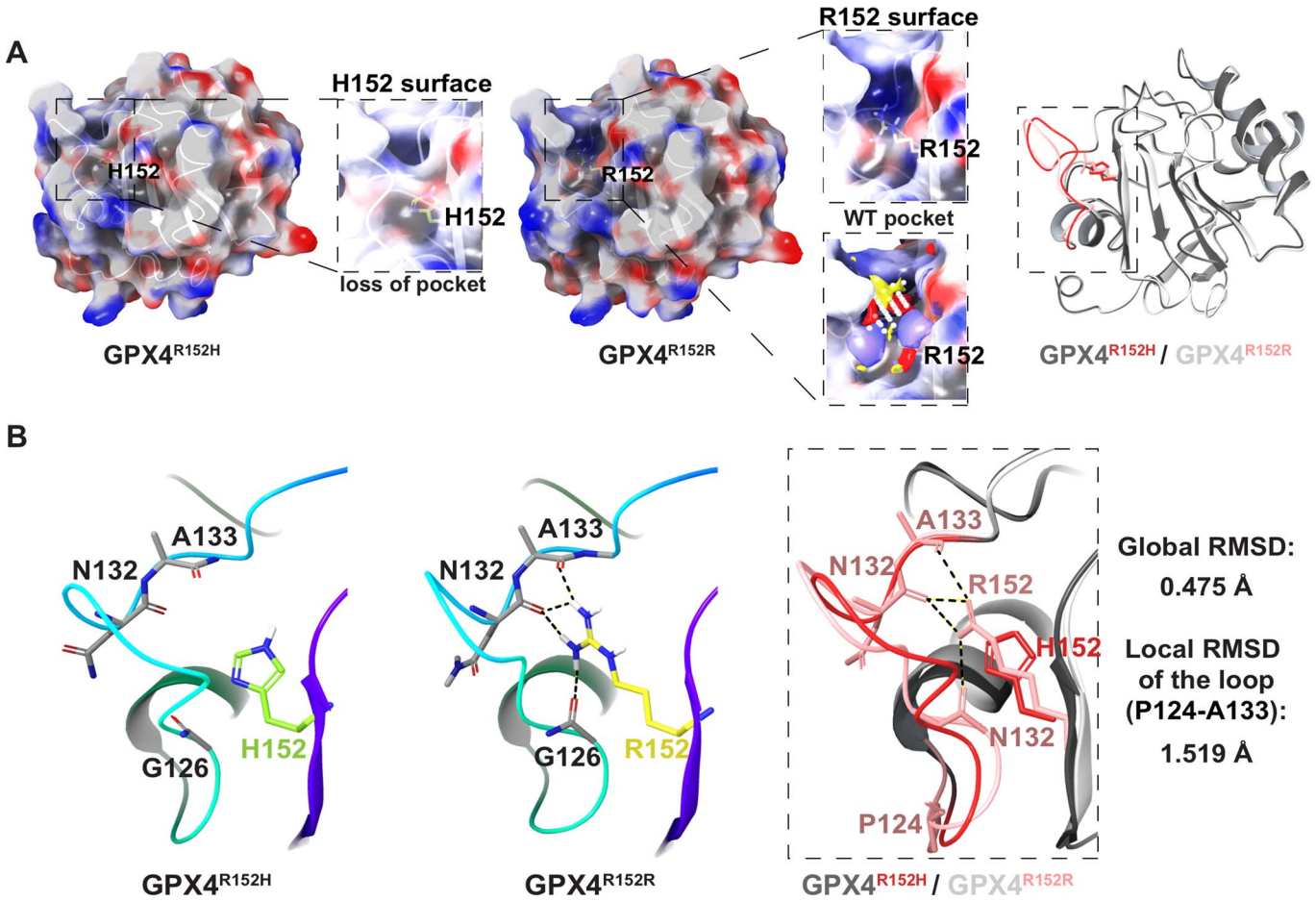

Extended Data Fig. 1 | *In silico* analysis of the impact of R152H mutation on GPX4 (GPX4^{U46C} PDB: 2OBI) structure. a, Structure of GPX4^{R152H} was computationally modeled based on the crystal structure of GPX4^{U46C} (PDB: 2OBI). As a control, structure of GPX4^{R152R} was also computationally modeled using the same algorithm, which indeed represents WT GPX4 but excludes artifacts from computational process when compared with the modeled R152H protein structure. Technically the two modeled proteins are GPX4$^{U46C\text{-}R152H}$ and GPX4^{U46C}. Protein surface are colored as below: hydrophobic (white), positive charge (red), and negative charge (blue). To visualize the pocket on top of R152 in the GPX4^{R152R} structure, white dots were shown as indicator of space. Overlap of the R152H variant backbone with wild-type was performed in the panel on the right, where the major conformational change in the loop around His152 was colored (WT as in pale pink and R152H as in red). See Supplementary Note for rationale of using U46C GPX4. **b**, The alternation of surface mainly derived from an outstanding conformational change of the loop between Pro124 and Ala133, with which the side chains of Arg152 formed multiple hydrogen bonds in the wild-type, but not His152 in the mutant.

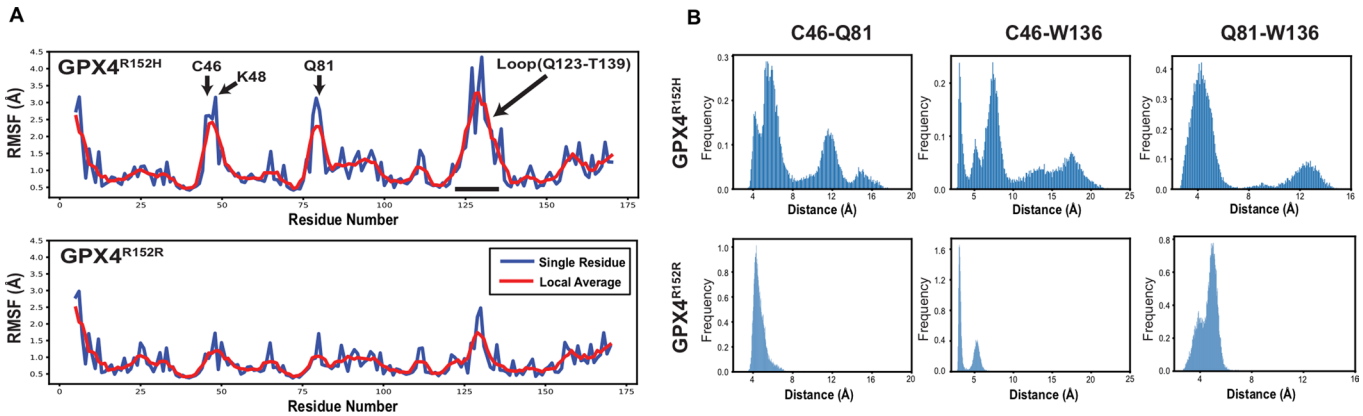

Extended Data Fig. 2 | Molecular Dynamic (MD) simulation analysis of the impact of R152H mutation on GPX4. a, RMSF of each residue in MD simulation based on the modeled GPX4 structure. Representative data from 5 times 100 ns trajectories were plotted. **b**, Distances between Cys46 and its catalytic partners Gln81/Trp136 were monitored in the MD simulation of GPX4^{R152H}, as compared to GPX4^{R152R}. Representative data from 5 times 100 ns trajectories were plotted.

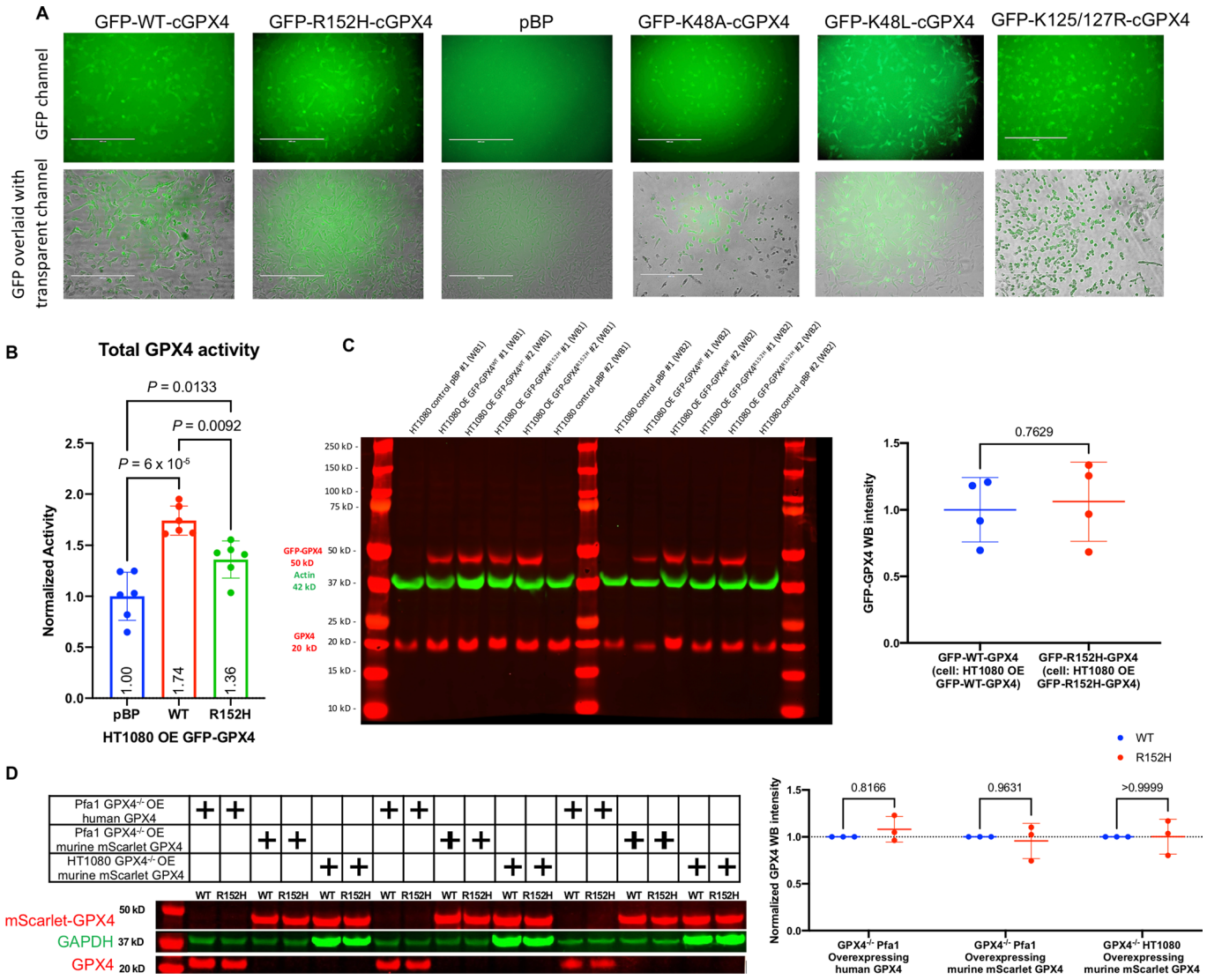

Extended Data Fig. 3 | Preparation of cell models of GPX4^{R152H}. a, HT-1080 transfected with pBP GFP-cGPX4^{WT}, pBP GFP-cGPX4^{R152H}, pBabepuro (pBP) empty vector, pBP GFP-cGPX4^{K48A}, pBP GFP-cGPX4^{K48L} and pBP GFP-cGPX4$^{K125R-K127R}$ were selected with puromycin and imaged with microscope. Triplicate experiments were repeated independently with similar results while the representative images were shown. The plotted scale bar is 400 μm. **b**, Total GPX4 enzymatic activity (endogenous apo-GPX4 and transfected exogenous GFP-tagged-GPX4) of control HT1080 (pBP, no expression of GFP-tagged-GPX4) and HT1080 cells overexpressing GFP-GPX4^{WT} or GFP-GPX4^{R152H}. Data are plotted as means ± SD of six replicate experiments. Ordinary one-way ANOVA followed by Tukey's multiple comparisons test was performed: n = 6, DF = 15 and P values were plotted. **c**, Western blot of control HT1080 (pBP) and HT1080 cells overexpressing GFP-GPX4^{WT} or GFP-GPX4^{R152H} using GPX4 and GAPDH antibodies. Expression levels of GFP-WT-GPX4 and GFP-R152H-GPX4 were quantified. Data are plotted as means ± SD, n = 4 biologically independent samples. Unpaired two-tailed t test was then performed and plotted: t = 0.3158, df=6, P^{ns} = 0.7629. **d**, Western blot of Gpx4-knockout Pfa1 cells overexpressing exogenous human WT or R152H GPX4, Gpx4-knockout Pfa1 cells overexpressing exogenous murine WT or R152H mScarlet-tagged GPX4, and Gpx4-knockout HT1080 cells overexpressing exogenous murine WT or R152H mScarlet-tagged GPX4 using GPX4 and GAPDH antibodies. Expression levels of GPX4 were quantified. Data are plotted as means ± SD, n = 3 biologically independent samples. Ordinary two-way ANOVA followed by Sidak's multiple comparisons test was performed and P values were plotted: n = 3, DF = 12. Full scan image is shown in the Supplementary Information.

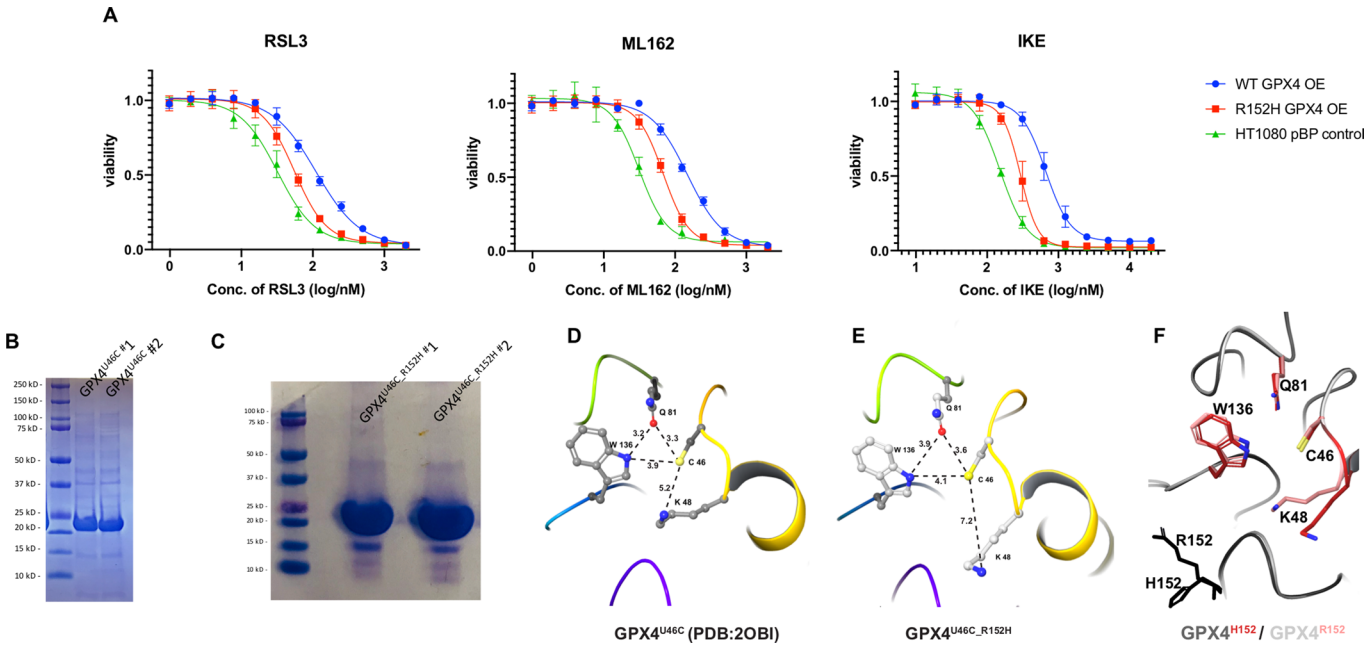

Extended Data Fig. 4 | Characterization of GPX4^{R152H} in cells and *in vitro*. a, HT1080 overexpressing exogenous WT or R152H GFP-GPX4 and a control line were tested for RSL3, ML162, and IKE sensitivity. Data are plotted as means ± SD, n = 3 biologically independent samples. **b-c**, SDS-PAGE gel of His-tagged GPX4^{U46C} and GPX4^{U46C_R152H} as stained by Coomasie Blue. Biologically independent duplicate experiments were performed and imaged. **d-e**, Distances between the catalytic triad in R152H variant were measured and labeled as compared to GPX4^{U46C} (PDB:2OBI). **f**, Shift of Lys48 away from the active site in the GPX4^{R152H} was plotted.

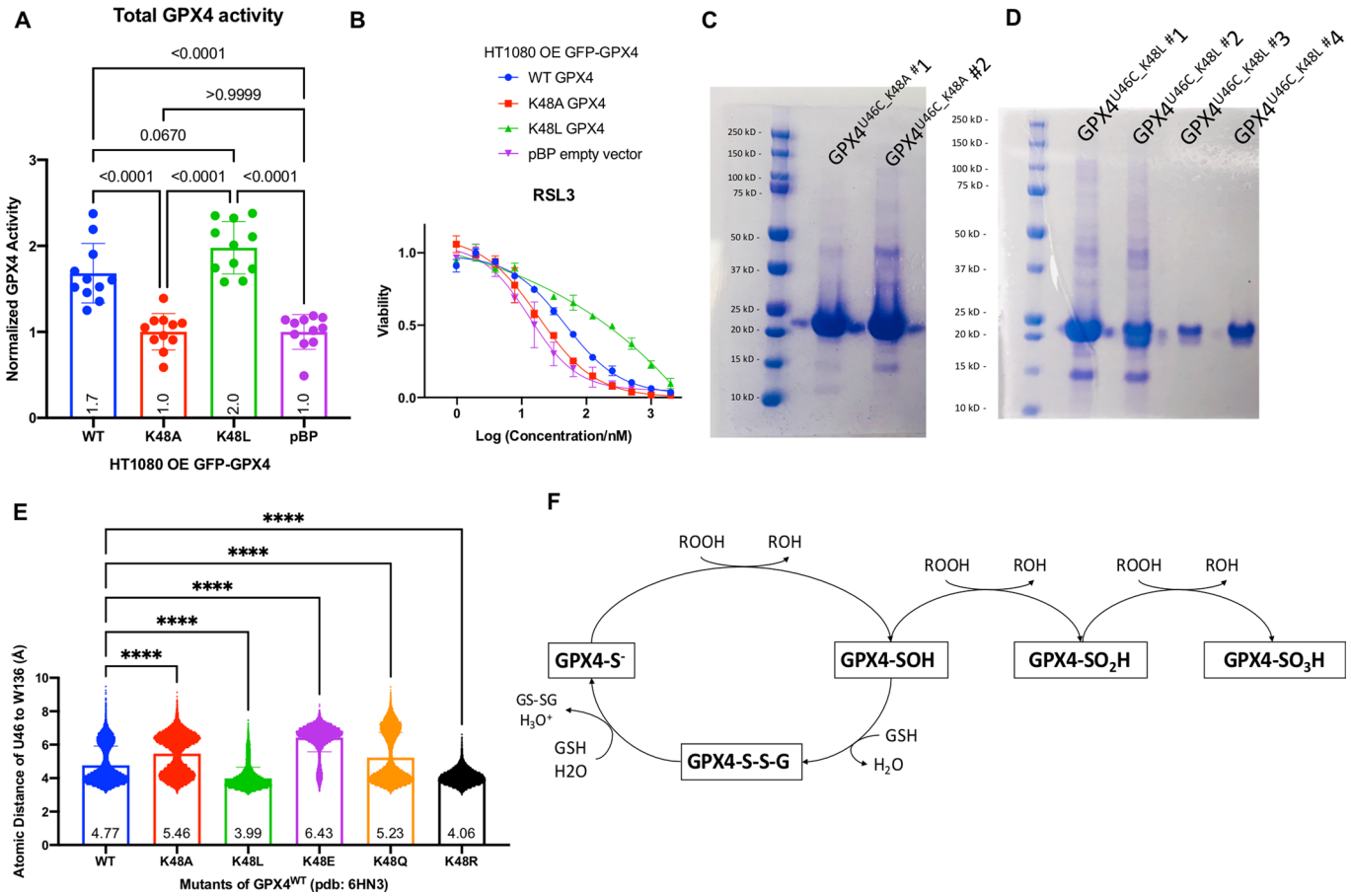

Extended Data Fig. 5 | Characterization of Lysine 48 mutants of GPX4 *in cells* and *in vitro*. a, Total GPX4 activity of HT1080 cells overexpressing GFP-GPX4^{WT}, GFP-GPX4^{K48A}, or GFP-GPX4^{K48L} and a control line. Data are plotted as means ± SD of eleven biologically independent replicate experiments. Ordinary one-way ANOVA followed by Tukey's multiple comparisons test was performed and P values were plotted, n = 11, DF = 40. **b**, HT1080 overexpressing exogenous WT, K48A, or K48L GFP-GPX4 and a control line were tested for RSL3 sensitivity. Data are plotted as means ± SD of three biologically independent replicate experiments. **c-d**, SDS-PAGE gel of His-tagged GPX4^{U46C_K48A} and GPX4^{U46C_K48L} as stained by Coomasie Blue. Biologically independent duplicate (GPX4^{U46C_K48A}) and quadruplicate (GPX4^{U46C_K48L}) experiments were performed and imaged. **e**, The distances between catalytic residues Sec46 and Trp136 were recorded every 4.8 ps throughout MD simulations of GPX4^{WT} (PDB: 6HN3), GPX4^{K48A}, GPX4^{K48L}, GPX4^{K48E}, GPX4^{K48Q}, and GPX4^{K48R}. Representative data from three times 100 ns trajectories were plotted as means ± SD. Ordinary one-way ANOVA followed by Tukey's multiple comparisons test was performed: n = 20835, DF = 125004, all P**** < $1x10^{-20}$. **f**, Scheme illustrating the catalytic cycle of sulfur-containing variant of GPX4.

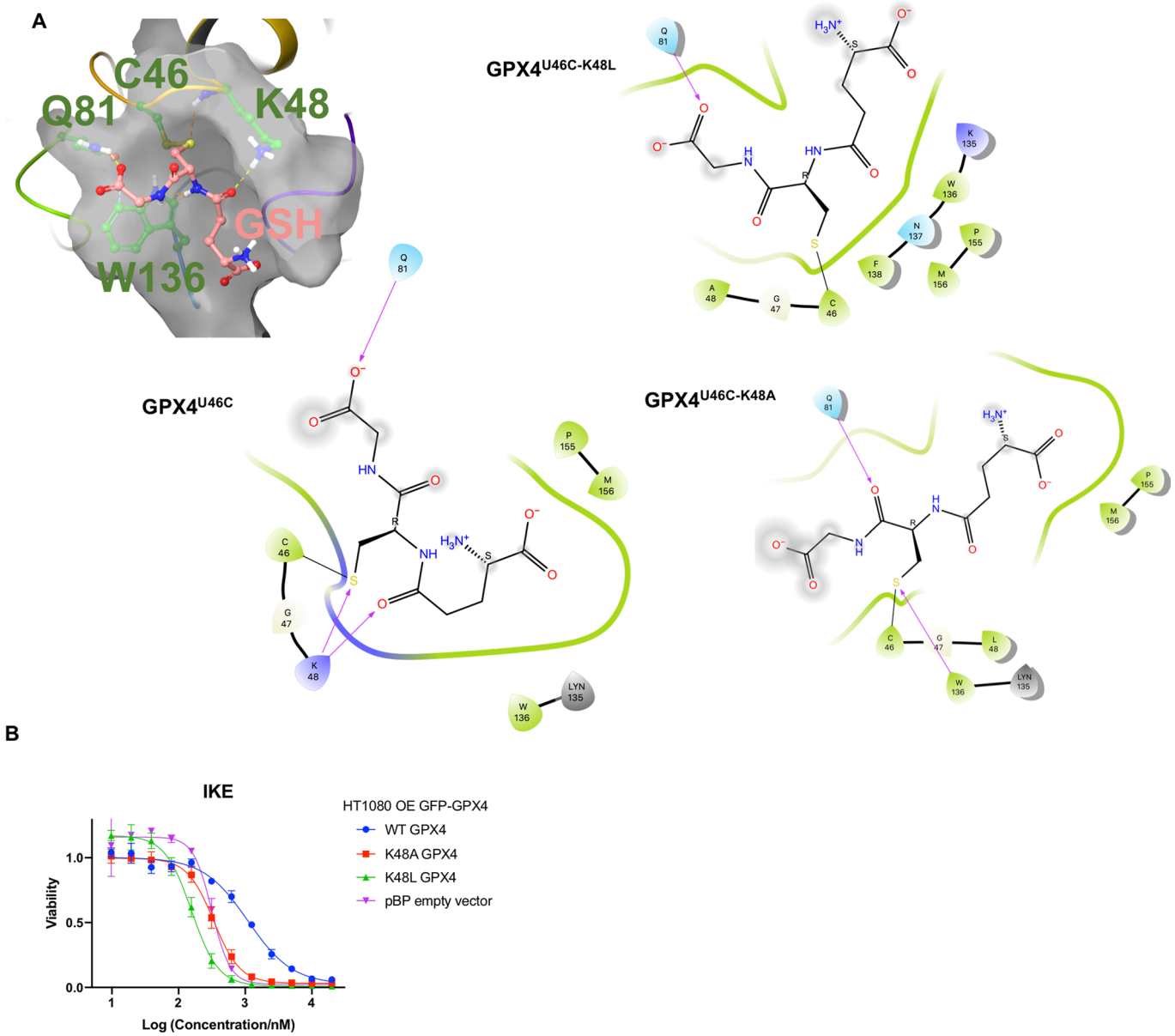

Extended Data Fig. 6 | Characterization of Lysine 48 mutants of GPX4 *in silico*. a, In silico docking of GSH to GPX4^{U46C}, GPX4^{K48A}, or GPX4^{K48L}. Top covalent-docking pose of GSH on GPX4^{U46C} (top left). 2D Ligand interaction diagram of GSH with GPX4^{U46C}, GPX4^{K48A}, or GPX4^{K48L} in their individually top covalent-docking pose (top right and bottom panels). **b**, HT1080 overexpressing exogenous WT, K48A, or K48L GFP-GPX4 and a control line were tested for IKE sensitivity. Data are plotted as means ± SD of three biologically independent replicate experiments.

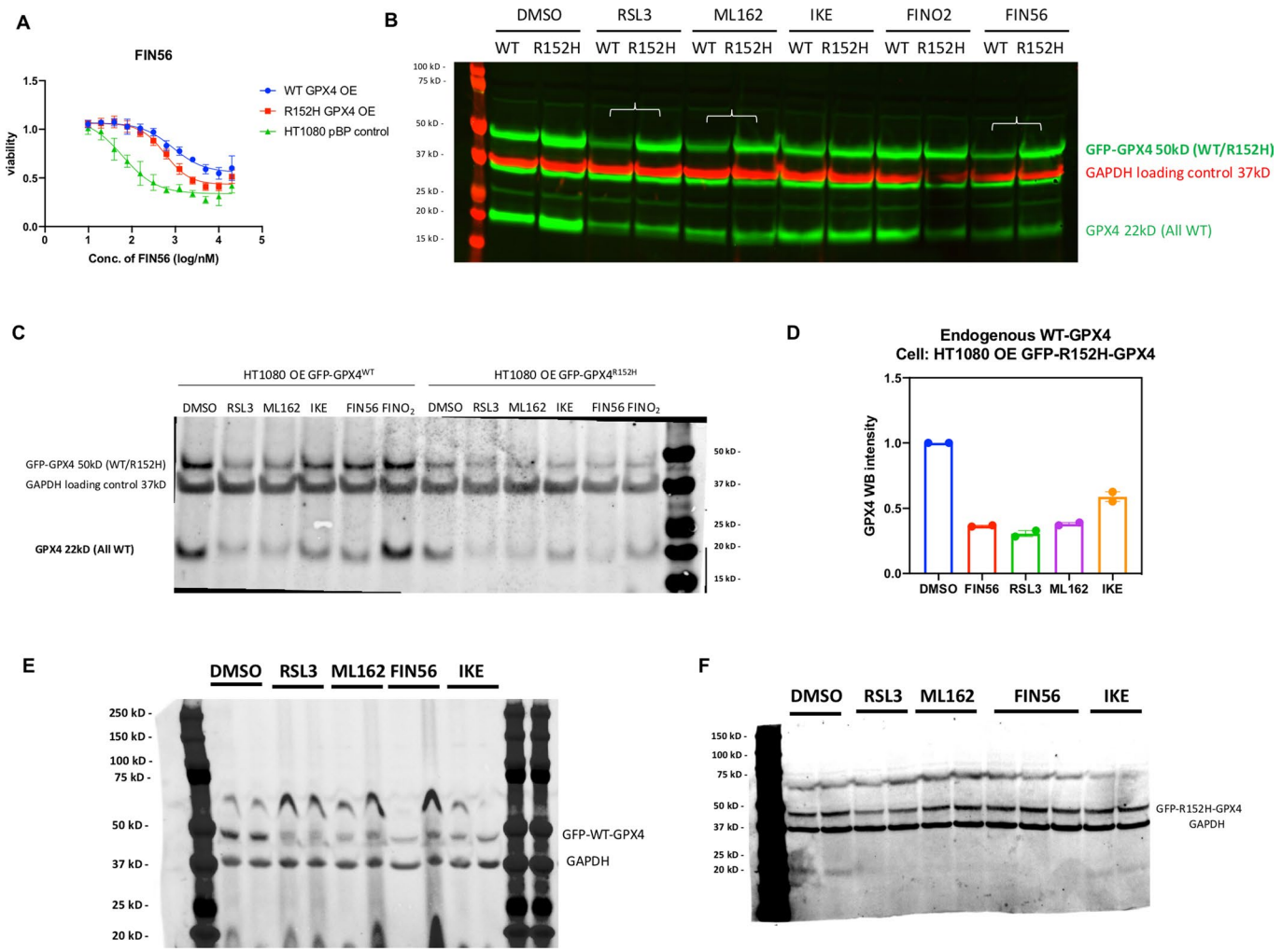

Extended Data Fig. 7 | Investigation of GPX4 degradation mechanism after treatment with ferroptosis inducers. a, HT1080 overexpressing exogenous WT or R152H GFP-GPX4 and a control line were tested for FIN56 sensitivity. Data are plotted as means ± SD, n = 3 biologically independent samples. **b**, Western blot of HT1080 OE GFP-GPX4^{WT} and HT1080 OE GFP-GPX4^{R152H} after treatment with ferroptosis inducers with GPX4 and GAPDH antibodies, with lanes arranged for cell line comparison. Triplicate experiments were repeated independently with similar results, which were shown in Extended Data Fig. 7c,e,f. **c**, Western blot of HT1080 OE GFP-GPX4^{WT} and HT1080 OE GFP-GPX4^{R152H} after treatment with ferroptosis inducers with GPX4 and GAPDH antibodies, with lanes arranged for ferroptosis inducer comparison. Triplicate experiments were repeated independently with similar results, which were shown in Extended Data Fig. 7b,e,f. **d**, The endogenous GPX4 in HT1080 OE GFP-R152H-GPX4 were tested for vulnerability to the degradation induced by RSL3, ML162, FIN56, and IKE. Data are plotted as means with range of two biologically independent experiments. The corresponding blots are shown in Extended Data Fig. 7b,c. **e**, Western blot of HT1080 OE GFP-GPX4^{WT} after treatment with ferroptosis inducers with GPX4 and GAPDH antibodies. Triplicate experiments were repeated independently with similar results, which were shown in Extended Data Fig. 7b,c. **f**, Western blot of HT1080 OE GFP-GPX4^{R152H} after treatment with ferroptosis inducers using GPX4 and GAPDH antibodies. Triplicate experiments were repeated independently with similar results, which were shown in Extended Data Fig. 7b,c.

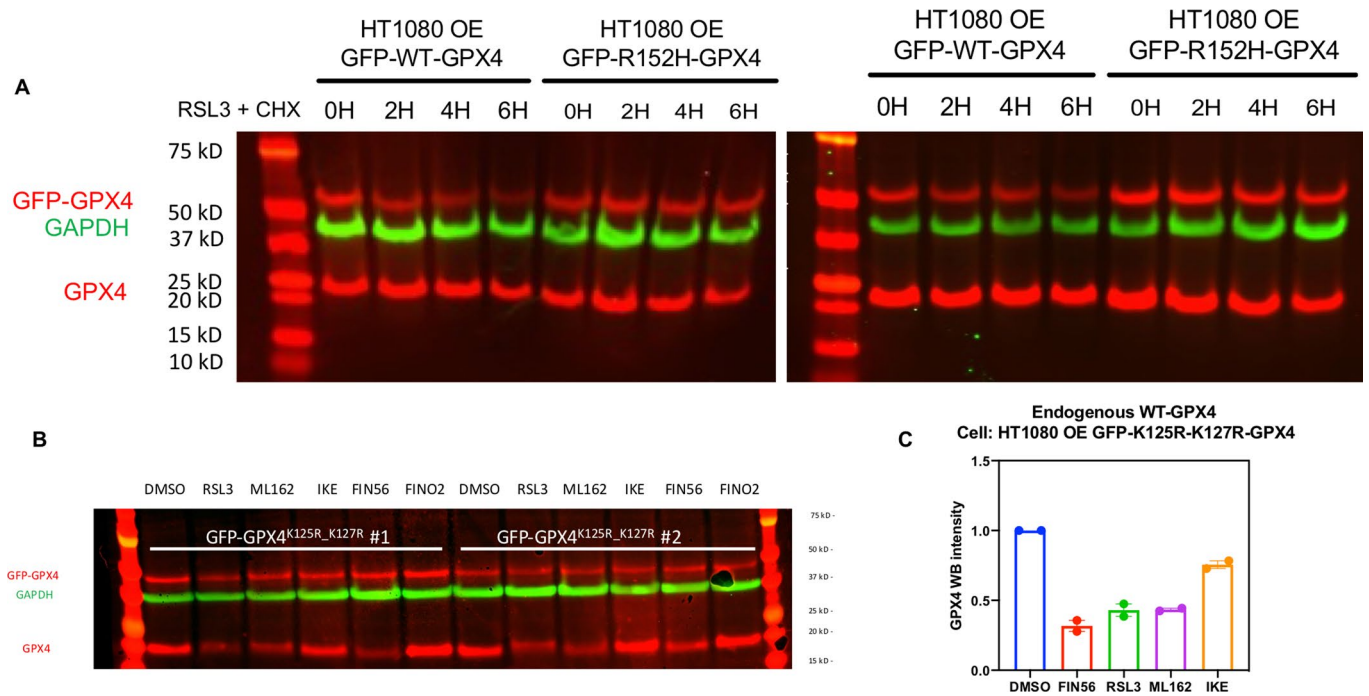

Extended Data Fig. 8 | Kinetic and mutagenesis study of GPX4 degradation mechanism after treatment with ferroptosis inducers. a, HT1080 OE GFP-GPX4^{WT} and HT1080 OE GFP-GPX4^{R152H} were treated with 4 μM RSL3, 30 μg/ml cycloheximide, and 100 μM a-Tocopherol for 0, 2, 4, or 6 hours before Western Blot analysis of GPX4 and GADPH. Biologically independent duplicate experiments were performed and imaged. **b**, Western blot of HT1080 OE GPX4^{K125R_K127R} after treatments with ferroptosis inducers using GPX4 and GAPDH antibodies. Duplicate experiments were performed and imaged. **c**, The endogenous GPX4 in HT1080 OE GFP-K125R-K127R-GPX4 were tested for vulnerability to the degradation induced by RSL3, ML162, FIN56, and IKE. Data are plotted as means with range of two biologically independent experiments. The corresponding blots are shown in Extended Data Fig. 8b.

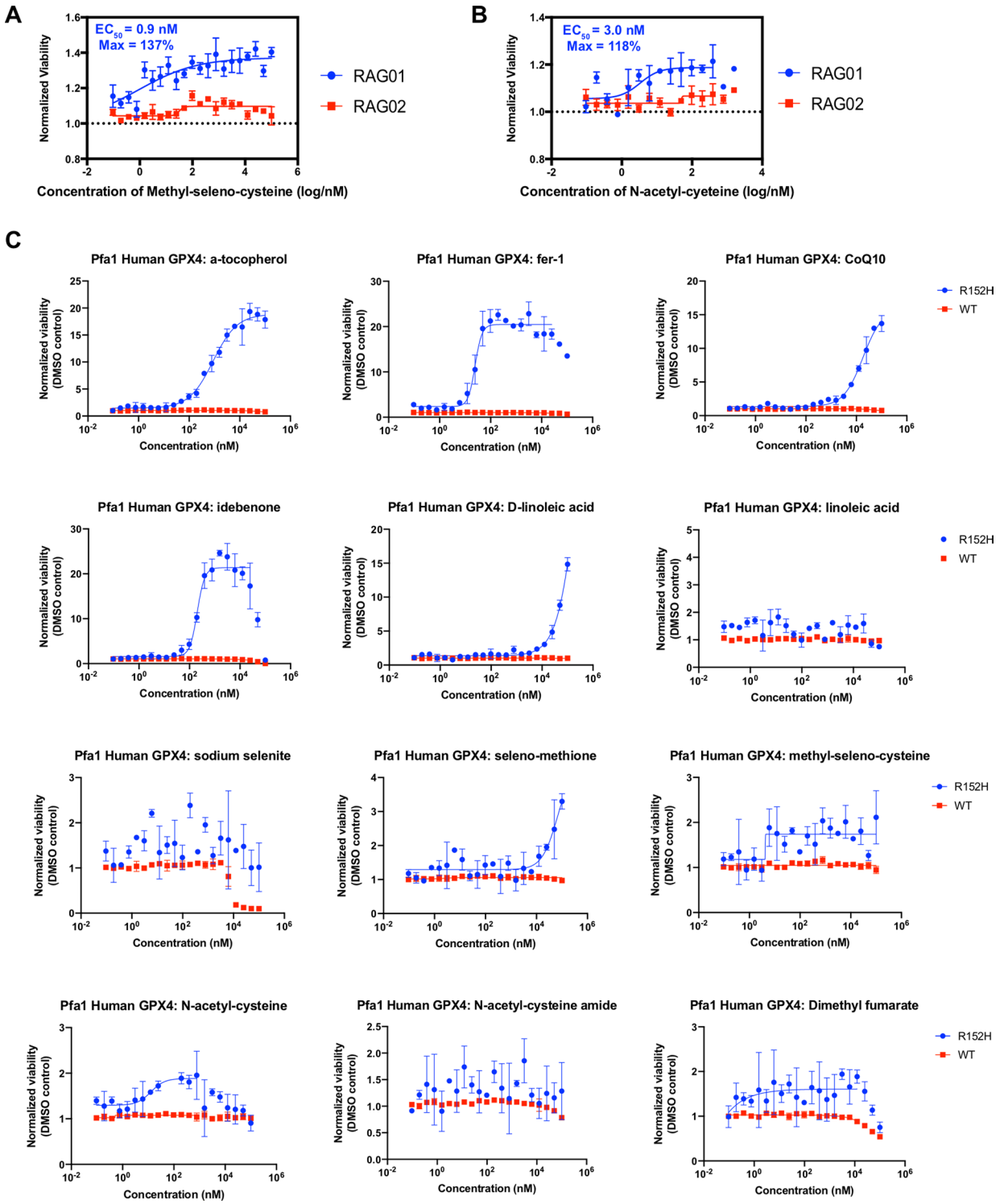

Extended Data Fig. 9 | Proof-of-concept treatments were tested on patient fibroblasts and Pfa1 cells, which were knocked out of endogenous GPX4 and transfected to overexpress human mScarlet-tagged GPX4^{WT} (red) or GPX4^{R152H} (blue). a-b, Supplementations of methyl-seleno-cysteine and N-acetyl-cysteine were tested as proof-of-concept treatments on the patient and control fibroblasts. Data are plotted as means ± SD (n = 3 biologically independent samples). **c**, Viability was normalized to the corresponding DMSO control. Data are plotted as means ± SD (n = 3 biologically independent samples). See Supplementary Note for effects of α-tocopherol.

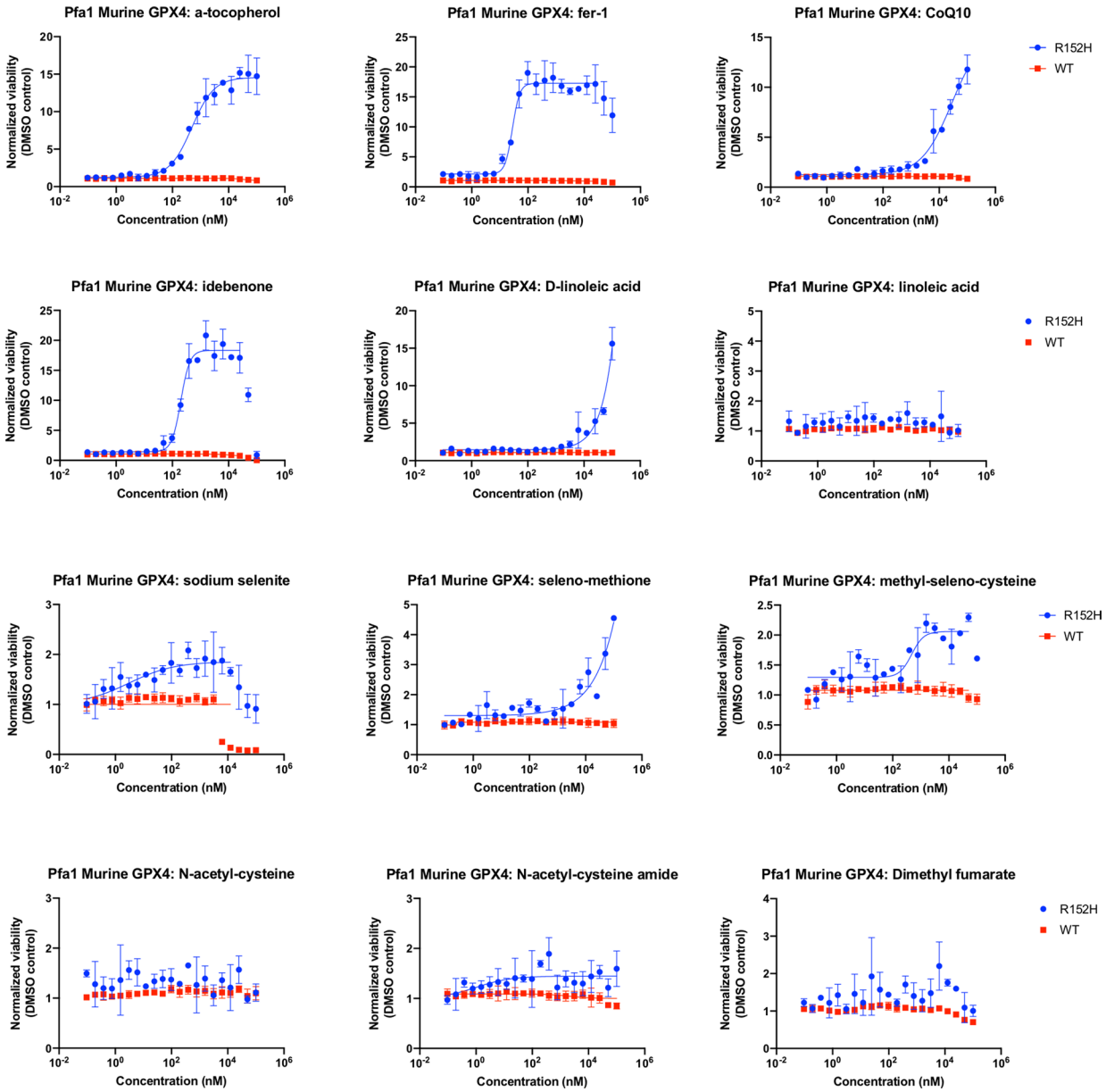

Extended Data Fig. 10 | Proof-of-concept treatments were validated in Pfa1 cells, which were knocked out of endogenous GPX4 and transfected to overexpress murine mScarlet-tagged GPX4^{WT} (red) or GPX4^{R152H} (blue). Viability was normalized to the corresponding DMSO control. Data are plotted as means ± SD (n = 3 biologically independent samples). See Supplementary Note for effects of α-tocopherol.

nature research

Corresponding author(s): Brent R. Stockwell

Last updated by author(s): Sep 20, 2021

Reporting Summary

Nature Research wishes to improve the reproducibility of the work that we publish. This form provides structure for consistency and transparency in reporting. For further information on Nature Research policies, see our Editorial Policies and the Editorial Policy Checklist.

Statistics

For all statistical analyses, confirm that the following items are present in the figure legend, table legend, main text, or Methods section.

n/a	Confirmed
☐	☒ The exact sample size (*n*) for each experimental group/condition, given as a discrete number and unit of measurement
☐	☒ A statement on whether measurements were taken from distinct samples or whether the same sample was measured repeatedly
☐	☒ The statistical test(s) used AND whether they are one- or two-sided *Only common tests should be described solely by name; describe more complex techniques in the Methods section.*
☒	☐ A description of all covariates tested
☒	☐ A description of any assumptions or corrections, such as tests of normality and adjustment for multiple comparisons
☐	☒ A full description of the statistical parameters including central tendency (e.g. means) or other basic estimates (e.g. regression coefficient) AND variation (e.g. standard deviation) or associated estimates of uncertainty (e.g. confidence intervals)
☐	☒ For null hypothesis testing, the test statistic (e.g. *F*, *t*, *r*) with confidence intervals, effect sizes, degrees of freedom and *P* value noted *Give P values as exact values whenever suitable.*
☒	☐ For Bayesian analysis, information on the choice of priors and Markov chain Monte Carlo settings
☒	☐ For hierarchical and complex designs, identification of the appropriate level for tests and full reporting of outcomes
☒	☐ Estimates of effect sizes (e.g. Cohen's *d*, Pearson's *r*), indicating how they were calculated

Our web collection on statistics for biologists contains articles on many of the points above.

Software and code

Policy information about availability of computer code

Data collection	Schrodinger Maestro (v.12.4.079) was used for computational modeling; The geometry of each crystal structure was fixed using programs XtalView (v4-1) and COOT (v0.8.9.2), and refined by Phenix (v1.17.1-3660).
Data analysis	ImageJ (v1.51) was used for Western Blot quantification; GraphPad Prism 9 was used for AUC analysis, line fitting, statistical analysis, and data plotting; The quantification of the immuno-fluorescence intensity was done using CellProfiler (v.3.1.8). Protein Thermal ShiftTM (v1.3) was used to analyze protein melting temperature.

For manuscripts utilizing custom algorithms or software that are central to the research but not yet described in published literature, software must be made available to editors and reviewers. We strongly encourage code deposition in a community repository (e.g. GitHub). See the Nature Research guidelines for submitting code & software for further information.

Data

Policy information about availability of data

All manuscripts must include a data availability statement. This statement should provide the following information, where applicable:

- Accession codes, unique identifiers, or web links for publicly available datasets
- A list of figures that have associated raw data
- A description of any restrictions on data availability

Structural data for GPX4 has been deposited in the Protein Data Bank (PDB), with accession codes PDB IDs: 7L8K, 7L8L, 7L8M, 7L8R, and 7L8Q. These structures will be made publicly available upon publication. Publicly available datasets used in this study are: PDB IDs: 2OBI, 6HN3. Source data are provided with this paper.

Field-specific reporting

Please select the one below that is the best fit for your research. If you are not sure, read the appropriate sections before making your selection.

☒ Life sciences ☐ Behavioural & social sciences ☐ Ecological, evolutionary & environmental sciences

For a reference copy of the document with all sections, see nature.com/documents/nr-reporting-summary-flat.pdf

Life sciences study design

All studies must disclose on these points even when the disclosure is negative.

Sample size	Sample size calculations were not performed. Sample sizes for quantitative experiments are at least n=3. The only exception is western blot quantifications for protein degradation study, which were performed in duplicates. In all cases, these sample sizes were selected because the effect sizes were expected to be large enough to obtain statistical significance from small n values based on preliminary pilot experiments and our prior experiences with similar experiments.
Data exclusions	No data were excluded for analysis.
Replication	To ensure reproducibility of experimental findings, each assay was performed at least two times to confirm the results. In particular, at least three times molecular dynamic (MD) simulations with random seeding were performed for each system (Fig. 1c, d, 3e, g, Extended Data Fig. 2, 5e). Cell viability experiments were performed with at least three distinct replicates for each treatment group (Fig. 2d, 3b, h, 4a, 5c, 6, Extended Data Fig. 4a, 5b, 6c, 7a, 9, 10). GPX4 biochemical assay were carried out with at least three biological replicates for each treatment and these data were used to calculate mean values (Fig. 2a, c, 3a, 5b, Extended Data Fig. 3b, 5a). Western blot quantifications for protein level determinations (stand-alone study) were at least based on biological triplicates for each condition (Fig. 5a, Extended Data Fig. 3c, d). Western blot quantifications for degradation study (comparative study) were at least based on biological duplicates for each treatment (Fig. 4b-f, Extended Data Fig. 7b-f, 8). All above and additional replication information was stated in the legends of corresponding figures.
Randomization	Replicate molecular dynamic (MD) simulations were performed technically with random seedings in the computation program setting to generate diverse states of the protein structures being simulated. Imaging area of fibroblast cells under confocal microscope is randomly selected for unbiased analysis. Randomization was not relevant to other experiments, quantifications of which at an ensemble level are not subject to biased interpretation regardless of randomization in sample allocation.
Blinding	Blinding was not perform because the data we analyzed are not subject to biased interpretation.

Reporting for specific materials, systems and methods

We require information from authors about some types of materials, experimental systems and methods used in many studies. Here, indicate whether each material, system or method listed is relevant to your study. If you are not sure if a list item applies to your research, read the appropriate section before selecting a response.

Materials & experimental systems

n/a	Involved in the study
☐	☒ Antibodies
☐	☒ Eukaryotic cell lines
☒	☐ Palaeontology and archaeology
☒	☐ Animals and other organisms
☐	☒ Human research participants
☒	☐ Clinical data
☒	☐ Dual use research of concern

Methods

n/a	Involved in the study
☒	☐ ChIP-seq
☒	☐ Flow cytometry
☒	☐ MRI-based neuroimaging

Antibodies

Antibodies used	All antibodies were obtained from commercial vendors. GPX4 (for WB, Abcam, ab125066), GPX4 (for IF, Santa Cruz, sc-166570), GFP (Santa Cruz, sc-9996), actin (Cell Signaling, D18C11), GAPDH (Santa Cruz, sc-47724), goat anti-mouse IgG (H+L) Secondary Antibody conjugated with Alexa Fluor 594 (for IF, Thermo Fisher Scientific Cat# A-11032, RRID:AB_2534091), IRDye® 800CW Goat anti-Rabbit IgG Secondary Antibody (for WB, LI-COR, #926-33221) and Goat anti Mouse IgG (H+L) Secondary Antibody conjugated with Alexa Fluor 680 (for WB, Thermo Fisher Scientific Cat# A-21057)
Validation	1. GPX4 (for WB, Abcam, ab125066) was knockout validated for WB application for mouse and human (referenced by 165 publications, including Chen C et al. Cell Death Dis 12:65, 2021). 2. GPX4 (for IF, Santa Cruz, sc-166570) was validated for detection of GPx-4 of mouse, rat and human origin by WB, IP, IF, IHC(P) and ELISA (referenced by 24 publications, including Yamada, N., et al. 2020. Cell Death Dis. 11: 144.) 3. GFP (Santa Cruz, sc-9996) was validated for detection of GFP and GFP mutant fusion proteins (not species-specific by its nature) by

WB, IP, IF, FCM and ELISA (referenced by 2,794 publications, including Wang, W.F., et al. 2017. Nat Commun. 8: 363.)
4. actin (Cell Signaling, D18C11) was validated for detection of actin of human, mouse, rat and monkey origins by WB, IP, IF, FCM and ELISA (referenced by 62 publications, including Jacquelyn M Walejko, et. al. et al. 2021. Nat Commun.)
5. GAPDH (Santa Cruz, sc-47724) was validated for detection of GAPDH of human and mouse origin by WB, IP, IF and IHC (referenced by 2,281 publications, including Dehghan, E., et al. 2017. Nat. Commun. 8: 2223.)

Eukaryotic cell lines

Policy information about cell lines

Cell line source(s)	1. HT-1080 and Pfa-1 cells were obtained from ATCC. 2. Human fibroblast cell line RAG01 and RAG02 were developed from patient with homozygous R152H variant and his parent with heterozygous R152H variant. RAG01 and RAG02 cell lines are available for both commercial and academic use through CureGPX4.org, a patient organization dedicated to finding a treatment for SSMD disease.
Authentication	HT1080 and Pfa-1 cells were cells were from ATCC with authentication. The authentication was performed by morphology check under microscopes and growth curve analysis. Human fibroblast cells were developed from research participants by RUCDR Infinite Biologics, then directly allocated to the authors, and tested without further authentication.
Mycoplasma contamination	We confirm that all cells were tested as mycoplasma negative.
Commonly misidentified lines (See ICLAC register)	No commonly misidentified cell lines were used in the study.

Human research participants

Policy information about studies involving human research participants

Population characteristics	Whole-exome sequencing (WES) was performed on three patients with SSMD features, in which homozygous R152H variant of GPX4 was recurrently identified. Ages and gender of the three patients were summarized below: 9 months old for Patient 1 (male, May 2019), 7 years old for Patient 2 (male, Dec 2015), and 10 months old for Patient 3 (female, Dec 2015). (The above ages are as of sequencing, with sequencing time denoted) Human fibroblast cell line RAG01 and RAG02 were developed from Patient 1 with homozygous R152H variant and his parent with heterozygous R152H variant: RAG01 - 22 months old, male, Patient 1 RAG02 - 31 years old, male, parent of Patient 1, control (The above ages are as of sample collection)
Recruitment	Patient 1 (Family 1) was transferred to Seattle Children's Hospital (Seattle, WA, USA) at day of life 6, when he was evaluated and found to have multiple congenital abnormalities. Later as SSMD features were observed on Patient 1, WES sequencing of Patient 1 was performed and a homozygous R152H variant in GPX4 was then identified. He was therefore recruited to this study. Patient 2 and 3 (Family 2) were presented to the Biochemical Genetics Clinic (San Diego, CA, USA) for additional diagnostic evaluation after WES was obtained. Considering their SSMD clinical features and the concurrent R152H variant in GPX4, they were therefore recruited to this study. As of the time of this study, Family 1 and 2 were the only families with patients of homozygous R152H variant known to the authors. They were therefore all included into this study. No self-selection/exclusion of human research participant or related bias was presented.
Ethics oversight	All three patients and their families (Patient 1 from Family 1, and Patient 2 and 3 from Family 2) gave informed consent for genetic and clinical investigation. Both families were enrolled in an institutional approved study of children with undiagnosed neurogenetic disorders (Genomic Sequencing in Neurological Disorders research protocol, UCSD IRB #170437). Tissue samplings (including skin biopsy for the development of fibroblasts RAG01 and RAG02) and clinical observations of Patient 1 and his parent were approved by IRB #00002259 (Molecular and Biochemical Analysis of Metabolic Disorders, University of Washington). Study of GPX4 variant in the human fibroblast samples was approved by IRB #AAAS9249 (Evaluation of GPX4 variant activity in fibroblasts, Columbia University). Compensations were not provided.

Note that full information on the approval of the study protocol must also be provided in the manuscript.